Chapter 2
High-T_c Films: From Natural Defects to Nanostructure Engineering of Vortex Matter

Roger Wördenweber

Abstract Due to their unique properties, ceramic high-T_c materials offer new perspectives for cryoelectronic applications. However, the 2D-layered structure in combination with the extremely small coherence length imposes extreme demands on the preparation of virtually single crystalline high-T_c films and the handling and manipulation of magnetic flux in devices made from these films. In this chapter, we will give an overview on vortex matter, pinning mechanism, vortex mobility, and vortex manipulation in high-T_c thin films. Vortex manipulation via artificially introduced structures will be demonstrated, and their potential for application in superconducting magnetometer and microwave devices will be sketched.

2.1 Introduction

Since the discovery of the first high-temperature superconductors (HTSs) [1], significant effort has been put into the research and realization of HTS thin film devices. On the one hand, this effort is motivated by the unique properties of HTS materials (e.g. the 2D nature or the elevated temperature up to which superconductivity persists lead to new phenomena); on the other hand, these superconductors offer new perspectives for application of cryoelectronic devices at elevated temperature.

The technology of devices and integrated circuits fabricated from low-temperature superconductors capable of operating at or near the temperature of liquid helium (4.2 K) is by now well established. A number of technical applications of HTS thin films [mainly passive (linear) and active (nonlinear) devices or electronic circuits] seem to have already a firm implementation base within the next years, and others represent tentative "dreams" for a more distant future. Typical application areas included: metrology and electronic instrumentation, radio astronomy and environmental spectroscopy (atmosphere and space), neurology and medical diagnostics, electronic warfare (radar, electronic countermeasures – ECM, magnetic anomaly detection), non-destructive materials evaluation (NDE/NDT), geological and environmental prospecting, telecommunication, ultrafast digital signal and data processing.

Nevertheless, the future application of HTS in cryoelectronic devices that are capable of operating at temperatures between typically 20 and 77 K will strongly depend on the solution of a number of problems. The major issues are:

1. The development of reproducible deposition technologies for high-quality single and multilayer HTS thin films and
2. The understanding and engineering of the superconducting properties (especially the critical properties)

Both issues are complicated by the complexity and the layered, quasi two-dimensional (2D) nature of the high-T_c superconductors.

In high-T_c material, the improvement of the superconducting properties (e.g. increase of T_c and increase of the energy gap ΔE) is accompanied by a significant enhancement of (Figs. 2.1 and 2.2):

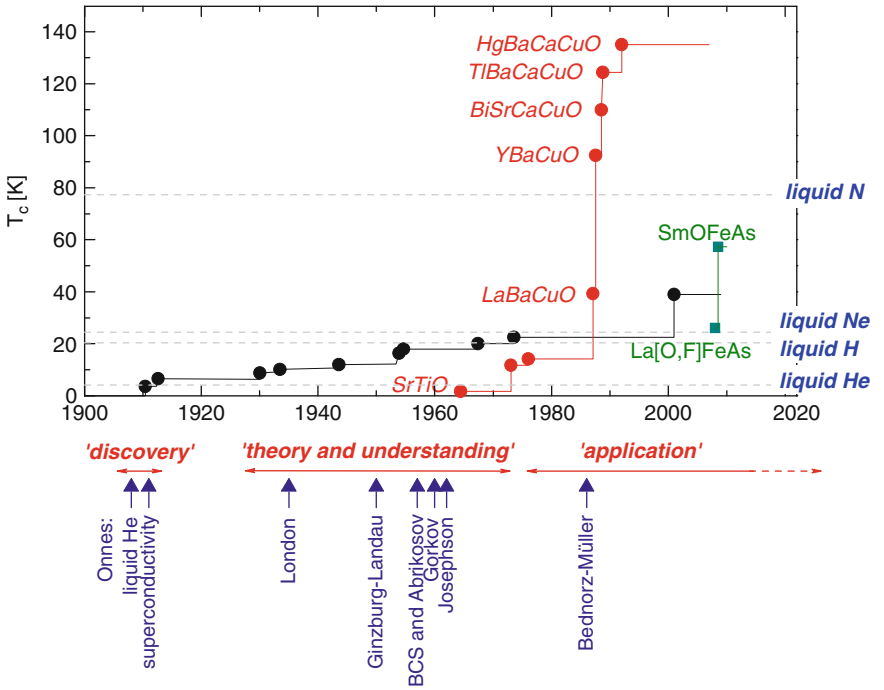

Fig. 2.1 Development of superconductivity: starting with the discovery of superconductivity in 1911 [2], the highest transition temperature T_c has been improved in time for metallic and metal compound superconductors (*black*), high-T_c ceramic superconductors (*red*) and, recently, ion arsenide-based layered superconductors (so-called pnictide superconductors, *green*). Organic superconductor (highest T_c present at 33 K for alkali-doped fullerene $RbCs_2C_{60}$ [3]) is not shown. Additionally, the normal boiling points of liquid cooling media are given, which indicate possible temperature regimes for application and major developments in discovery, theory, understanding and application are indicated

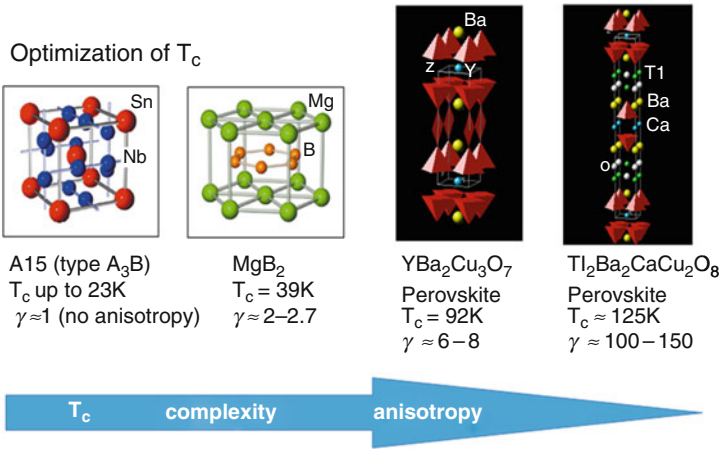

Fig. 2.2 The improvement of the superconducting properties (e.g. increase of T_c and energy gap ΔE) is achieved by an enhancement of complexity (structural as well as stoichiometric) and anisotropy of the superconductor. The HTS represents a quasi 2D-layered superconductor

1. The number of elements
2. The structural complexity
3. The anisotropy

The quasi 2D nature of the oxide superconductors related to their layered structure leads to a large anisotropy in nearly all parameters. It is characterized by the anisotropy factor

$$\gamma = \frac{\xi_{ab}}{\xi_c} = \frac{\lambda_c}{\lambda_{ab}}, \tag{2.1}$$

defined by the ratio of the coherence lengths ξ or penetration lengths λ measured for magnetic field applied in crystallographic a–b or c direction, respectively. Values of $\gamma \approx 6$–8 for $YBa_2Cu_3O_{7-\delta}$ (YBCO), $\gamma \approx 55$–122 for Bi compounds, and $\gamma \approx 100$–150 for Tl compounds are reported [4–7]. Furthermore, extremely small coherence lengths are determined for these superconductors. Values of $\xi_c = 0.02$–0.04 nm and $\xi_{ab} = 2$–2.5 nm ($Bi_2Sr_2CaCu_2O_{8+\delta}$), $\xi_c = 0.3$–0.5 nm, and $\xi_{ab} = 2$–3 nm ($YBa_2Cu_3O_{7-\delta}$) are measured, which, furthermore, strongly depend on sample quality and oxygen content [8]. Therefore, local variations in the sample properties on the scale of ξ will automatically result in a spatial variation of the superconducting properties. Due to the extremely small coherence length along the crystallographic c-axis, only the current directed along the crystallographic a–b direction (i.e. along the CuO_2 planes) represents a "superconducting current" and can be used for applications. Since misalignments in the a–b plane lead to grain boundaries that strongly affect the critical properties, perfect biaxial c-axis orientated epitaxial HTS films including the avoidance of anti-phase boundaries are necessary for most applications. This requires thin film growth with perfection on nanometre scale.

The electronic properties of superconducting devices are usually strongly determined or affected by the presence or motion of quantized magnetic flux (so-called flux lines or vortices) in the type-II superconductor. Most superconducting devices will (or have to) operate in magnetic fields strong enough to create large densities of vortices within the device. Generally flux penetrates the superconductor for magnetic fields $B > B_{c1}$, with the lower critical field B_{c1}. The demagnetization effect will lead to a considerable enhancement of the magnetic field at the edge of a superconductor sample.

Moreover, calculation of the Gibb's free energy for vortices in thin film devices using an approximation of the sample geometry by a rectangular cross-section with film thickness d (parallel to the magnetic field direction) much smaller than the lateral dimension w (in contrast to the elliptic approximation of the cross-section used in the classical picture) indicates [9] that (1) the first tunnelling of single vortices (e.g. via thermal-activated penetration) through the geometrical barrier at the edge of the superconductor is expected to occur already at extremely small fields

$$B_{\mathrm{T}} = \frac{d}{2w} B_{c1} \tag{2.2}$$

and (2) that collective penetration of vortices takes place at the penetration field

$$B_{\mathrm{P}} = \sqrt{\frac{d}{w}} B_{c1}. \tag{2.3}$$

These predictions are valid for most HTS devices and patterns, i.e. as long as $w \gg d > \lambda$ is valid. As a consequence, HTS films, devices and patterns are usually strongly penetrated by magnetic flux lines (Fig. 2.3).

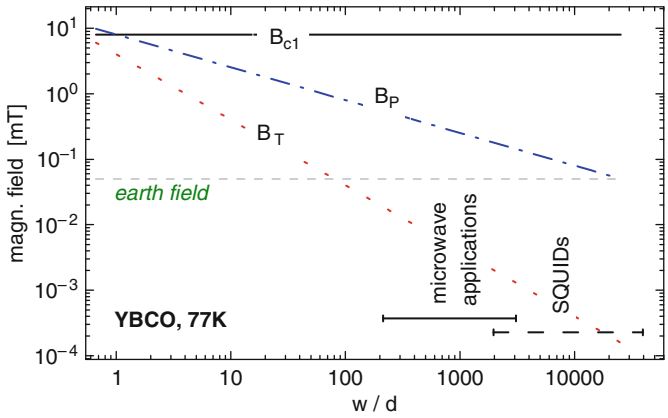

Fig. 2.3 Critical field B_{c1}, tunnelling field B_{T} and penetration field B_{P} as function of the reduced width for patterned YBCO films at 77 K. Typical regimes for cryogenic applications are indicated

The presence of vortices or its motion will lead to dissipative processes, flux noise or local modification of the superconducting properties of these devices. The performance of the device will be diminished. Due to the large anisotropy, the small coherence length and, last but not least, the elevated temperature at which the ceramic superconductors will be operated, these effects are even more severe for HTS material. Ways to avoid the impact of vortices are:

- Operation in perfectly shielded environments
- Reduction of the structures to nm size that does not allow for vortex formation
- "Manipulation" of vortex matter

Since the first two options are in most cases (extremely) costly and/or usually technically difficult or impossible, the manipulation of vortex matter appears to be an ideal solution for this problem. This is one of the motivations for scientific work on vortex manipulation in HTS thin films. Furthermore, the manipulation of vortices is of interest for the development of (novel) fluxon concepts and the understanding of vortex properties in general. In this chapter, an overview on different aspects of vortex manipulation and vortex matter in micro- and nanopatterned HTS films will be given.

2.2 Vortex Matter in High-T_c Superconductors

In order to understand vortex matter and vortex manipulation in micro- and nanopatterned HTS, one should first consider vortex matter in unpatterned type-II superconductors. This is done in the following sections. First, the impact of vortex motion on the electric properties of superconductors is discussed; then basic concepts of elementary vortex–defect interactions are sketched and, finally, different mechanisms of volume flux–flux pinning and flux motion are discussed. The intention of these sections is to provide the basic understanding of the mechanism of vortex motion and flux pinning in HTS material and to motivate different strategies to manipulate vortex motion and pinning in these complex materials.

2.2.1 Vortex Motion in Ideal Superconductors

If a vortex in an ideal superconductor is exposed to a driving force, it will start to move under the action of the force. The driving force can be provided for instance by an applied current (Lorentz force),

$$\vec{f}_{\text{vortex}} = \vec{J} \times \vec{\Phi}_{\text{o}}, \tag{2.4}$$

a temperature gradient or a magnetic field gradient. Furthermore, vortex motion can be assisted by a finite temperature (thermal activation or thermally assisted vortex

motion). Within a perfectly homogeneous system, the driving force is counteracted only by a friction force:

$$\vec{f}_{\text{vortex}} = -\eta\vec{v}, \tag{2.5}$$

with v denoting the steady-state velocity of the vortex. As a consequence of the flux motion, a finite electric field

$$\vec{E} = n_{\text{v}}\vec{\Phi}_o \times \vec{v} = \vec{B} \times \vec{v}, \tag{2.6}$$

is generated in the superconductor (n_{v} represents the sheet density of vortices). Thus, a steady flow of vortices in a device will result in a finite flux-flow resistance:

$$\rho_{\text{ff}} = \frac{\partial E}{\partial J} = \frac{\Phi_{\text{o}} B}{\eta}. \tag{2.7}$$

The electric field caused by vortex motion is one of the major problems of superconducting electronic devices operating in magnetic fields. An ideal (i.e. defect-free) superconducting wire would expose a resistance to an applied current (Fig. 2.4). Thermal activation of flux lines would lead to statistic fluctuations (i.e. statistic motion) of vortices even at low temperatures that would manifest itself by (flux or voltage) noise signals, e.g. telegraph noise in superconducting magnetometers [e.g. superconducting quantum interference device (SQUID), see Fig. 2.4].

2.2.2 Flux Pinning and Summation Theories

In order to retain the dissipation-free dc current or reduce the voltage noise due to vortex motion, flux lines have to be pinned by defects in the superconducting material (so-called pinning sites). The vortex–pin interaction of the defects compensates the driving force up to a critical value. In case of current driven vortex motion, the Lorentz force defines the maximum dissipation-free current density. The experimentally determined volume pinning force F_{p}, Lorentz force and critical current density J_{c} are correlated by:

$$\vec{F}_{\text{p}} = -\vec{F}_{\text{L}} = \vec{B} \times \vec{J}_{\text{c}}. \tag{2.8}$$

The volume pinning force is either obtained via summation of the elementary pinning force f_{p} (*pin-breaking mechanism*) or defined by the stability of the strongly pinned flux-line lattice (*flux-line shear mechanism*). Both mechanisms will be sketched below.

In general, mechanisms of volume flux pinning and flux motion in real type-II superconductors have to be discussed in four steps:

1. The *interaction between individual pinning centres and vortices* represents the basis of the vortex pinning.
2. The *interaction between individual vortices* defines the formation and properties of the vortex lattice as well as its reaction on driving forces and elementary pinning.

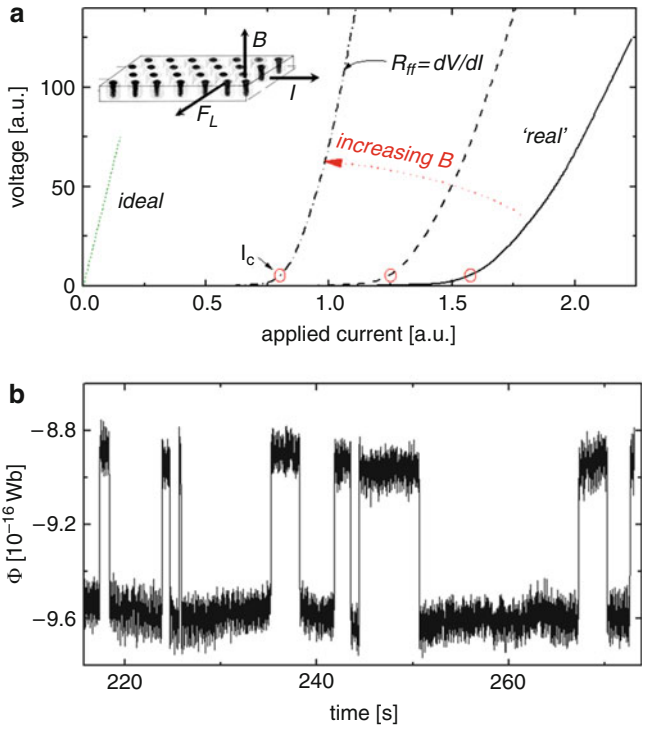

Fig. 2.4 (**a**) Schematic drawing of current–voltage characteristics for an ideal superconductor and a real superconductor at different applied fields. The critical current I_c (usually defined by a voltage criterion of 1 μV/cm) and the flux-flow resistance are indicated. The inset shows the vortex lattice and the directions of current, applied field and resulting Lorentz force for a superconducting thin film with B normal to the film surface. (**b**) Thermally activated flux noise in a HTS SQUID

3. Adequate summation of the effects of many pins usually at random position taking into account the vortex–pin interaction and the vortex–vortex interaction leads to the prediction of the maximum volume pinning force $F_{p,max}$ of the system.
4. Finally, the *homogeneity* of the superconducting material in terms of amplitude and length scale of the variation of the superconducting properties defines the resulting mechanisms of vortex motion and volume vortex pinning F_p.

Ad (1): The elementary vortex–pin interaction depends on the type of defect. It originates from the interaction between a vortex and an inhomogeneity or defects in the superconducting material. Real superconductors always posses "natural" defects (e.g. grain boundaries, dislocations, voids, precipitates) resulting in a finite critical current. Vortex–pin interactions can be classified in the following categories:

- *Geometrical* or morphological interaction (e.g. thickness variation and surfaces)
- *Magnetic* interaction arising from the interaction of superconducting and non-superconducting material (e.g. vacuum and extended precipitates) parallel to the

applied magnetic field. This interaction is determined by the field gradient in the superconductor, i.e. the penetration depth λ

- *Core* interaction arises from the coupling of locally distorted superconducting properties with the periodic variation of the superconducting order parameter. Neglecting the complicated case of pinning by spatial variation of the Fermi-surface or of magnetic properties, there exist only two predominant mechanisms for core pinning: δT_c – *pinning* (spatial variation of the density, elasticity or pairing interaction of the material) and $\delta\kappa$-*pinning* (variation of the electron mean free path)

The vortex–pin interaction depends on the gradient of the magnetic field or superconducting order parameter. In technical type-II superconductors, the magnetic penetration length λ is typically much larger than the superconducting coherence length ξ. Therefore, magnetic interaction does not play an important role for vortex pinning in these materials. In unpatterned type-II superconductors, *core pinning* and, especially, $\delta\kappa$-*pinning* dominate. The situation is slightly different for artificially induced defects. Typical candidates of artificial defects for thin film applications are *irradiation defects*, *magnetic* or *non-magnetic dots*, completely or partly etched holes (*antidots* or *blind holes*) [14, 15], specially patterned defects such as *moats*, *channels* [13, 25] and many more structures. Depending on the size (most artificial defects are larger than ξ and often even larger than λ), choice of material (vacuum, non-superconducting, metal, magnetic) and shape, different types of interactions (geometric, magnetic, core) or combinations of these interactions are present. In some cases, alternative mechanisms of interactions are present. For instance, magnetic field compensation defines the major interaction of magnetic dots and vortices. As an example, the elementary vortex–pin interaction of vortex–antidot interaction will be discussed in Sect. 2.3.2.

Ad (2): Vortices–vortex interaction leads to the formation of vortex lattices. With a driving force smaller than the volume pinning force (static vortex lattice and small pinning forces), the vortex lattice will be deformed due to the vortex–pin interaction. The deformation can be elastic or plastic, or instabilities can be formed [16, 17]. The different mechanisms are comparable to the reaction of solids upon internal stress. As long as the strain is small, the vortex lattice can reach its equilibrium position with respect to the pin distribution without plastic shear taking place in the lattice. In case of larger strain, plastic shear will create a significant number of flux-line defects. The combination of (1) and (2) leads to the deformation of the vortex lattice described by the displacement field. The deformation can be two-dimensional (transversal displacement) [16] or three-dimensional [17].

Ad (3): The adequate summation of the effects of many pins usually at random position leads to the prediction of the maximum volume pinning force, $F_{p,max}$, taking into account the elementary vortex interaction, the distribution and density of pinning sites and the kind of deformation in the vortex lattice. Note that this volume pinning force, $F_{p,max}$, is not automatically identical with the force $F_p = J_c B$, which is defined by the onset of vortex motion. The summation problem can be solved in some ideal or model systems. In the easiest case, every pinning centre is able to exert its maximum pinning force, f_p, on the vortex lattice, and the net volume

pinning force would be given by the *direct summation* [18]:

$$F_{p,DS} = -F_{p,max} = \sum \left(\frac{f_p}{V} \right). \tag{2.9}$$

This case is usually not observed in real (i.e. non-artificial) systems at moderate or large applied magnetic induction. In very small magnetic fields, for which the vortex lattice parameter $a_o = 1.075(\Phi_o/B)^{1/2} \gg \lambda$, direct summation is appropriate, since the vortex–vortex interaction is negligible. At higher fields, a totally flexible vortex lattice or a distribution of pin sites which is matched to the vortex lattice [14, 15] would be necessary to apply direct summation. The latter is for instance in case of commensurability of the vortex lattice with an artificial patterns (see Sect. 2.3.3.1).

The realistic scenario for real type-II superconducting material in moderate or large magnetic fields is different. The volume pinning force has to be evaluated for the case of larger correlated regions in the vortex lattice via adequate summation of the elementary vortex–pin interactions. This summation of the elementary pinning forces of a realistic defect system has been a long standing problem which was first solved in the form of the theory of collective pinning [19]. Other approaches of the evaluation of correlation lengths due to small disorder in the vortex lattice caused by the vortex–pin interaction are discussed in the literature [20]. Modifications of the collective pinning theory have been introduced especially for HTS, assuming a system of point pins with typical dimensions smaller than ξ [21–23].

Ad (4): Finally, the mechanism of flux motion determines the onset of dissipation due to a driving force. This mechanism defines the irreversible properties, i.e. the experimentally determined volume pinning force F_p given by the critical current density J_c:

$$\vec{F}_p = \vec{J}_c \times \vec{B}, \quad \text{with } F_p \leq F_{p,max}. \tag{2.10}$$

The volume critical force F_p can differ strongly from the maximum volume pinning force $F_{p,max}$. It depends upon (1) the relation between vortex–vortex interaction and vortex–pin interactions and (2) the homogeneity of the superconductor on a length scale larger than the coherence length [24–27]. Thus, the mechanism of vortex motion strongly depends upon strength, density and distribution of pinning centres, on the elastic or plastic response of the vortex lattice, and the homogeneity of the superconducting material. The two different kinds of interactions (vortex–vortex and vortex–pin) in combination with the homogeneity of the superconductor automatically introduce two different mechanisms of vortex dynamic: *pin breaking* and *flux-line shear mechanisms*.

If the differences between depinning forces of neighbouring vortices are small compared to the vortex–vortex interaction, the complete vortex lattice will be pinned or depinned. This situation is referred to as *pin breaking*. The volume pinning is given by statistical summation of the elementary interactions in the correlation volume $V_c = L_c \, {R_c}^2$ [19]:

$$F_p = F_{p,PB} = F_{p,max} = \sqrt{\frac{n\left\langle f_p^2\right\rangle}{V_c}} = \sqrt{\frac{W(0)}{V_c}}. \tag{2.11}$$

Here n denotes the density of pinning sites, $W(0)$ represents the collective pinning parameter, and L_c and R_c are the correlation lengths perpendicular and parallel to the magnetic field direction, respectively. The resulting field dependence is shown in Fig. 2.5a for a weak-pinning type II superconductor (a-Nb_4Ge). Up to a given field, the elastic deformation of the vortex lattice sustains and the field dependence of the volume pinning force is nicely described by the collective pinning theory (2.11). At high fields, plastic deformations set in leading to an increase in the pinning force with respect to the predictions of the collective pinning theory. The so-called peak effect at high fields (Fig. 2.5a) is a characteristic feature of the collective pinning behaviour in weak pinning material.

When the local pinning force strongly varies over length scales comparable to or larger than the vortex–vortex distance, vortices or bunches of vortices will start to move independently as soon as the driving force exceeds the flow stress of the vortex

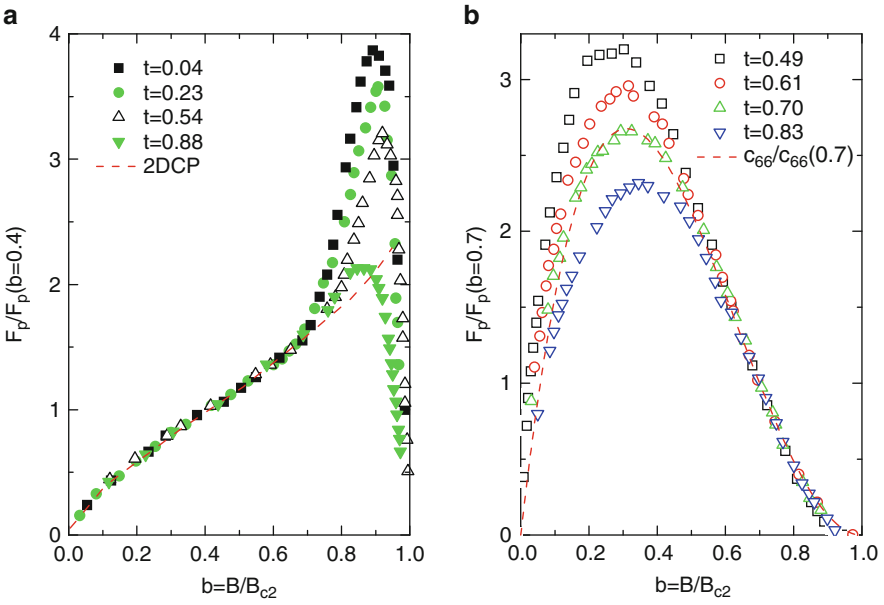

Fig. 2.5 Normalized volume pinning force as a function of applied magnetic induction for (**a**) *pin breaking mechanism* in weak pinning amorphous Nb_4Ge thin films with $F_p(b = 0.4)$ typically of the order of 10^5–10^6 N/m^3 at 2.2 K [16] and (**b**) *flux-line shear mechanism* in strong-pinning NbN thin films with $F_p(b = 0.7)$ typically of the order of 10^8–10^9 N/m^3 at 4.2 K [25]. The *dashed lines* represent the field dependence of 2D collective pinning theory with $L_c = d$ (**a**) and the shear module (**b**), respectively; d represents the film thickness, and t denotes the reduced temperature $t = T/T_c$

lattice. In the so-called flux-line shear mechanisms, the volume pinning force is determined by the vortex–vortex interaction. It is not given by the maximum volume pinning force $F_{p,max}$ of the weak or strong pinning areas, but it is determined by the plastic shear properties of the vortex lattice, since areas, that are weakly pinned, shear away from strongly pinned regimes. The resulting volume pinning force for the *flux-line shear mechanisms* is given by [24–27]:

$$F_p = F_{p,FLS} = G\, c_{66} \propto \frac{B_{c2}^2}{w} b(1-b)^2, \tag{2.12}$$

with $c_{66} \propto B_{c2}^2 b(1-b)^2$ representing the shear modulus of the vortex lattice, G a geometrical factor, $b = B/B_{c2}$ the reduced field, and B_{c2} the upper critical field. The typical field dependence obtained for a strong pinning superconductor is shown in Fig. 2.5b. It is characterized by a broad peak at small magnetic field typically at $B \approx B_{c2}/3$. The flux-line shear mechanism is usually encountered in strong pinning (i.e. technical) systems, whereas weak pinning superconductors often show collective pinning behaviour.

2.2.3 Pinning Mechanism in HTS

Bearing in mind the small coherence length and anisotropy, high-T_c material clearly shows a flux pinning according to the *flux-line shear mechanisms*. Vortices move in weak pinning "channels" when the critical current is exceeded. The field dependence of F_p shows the typical peak at small field, and it can be described by the field dependence of the flux-line shear mechanism (2.12), additionally taking into account the impact of thermal activation and/or a distribution in the channel properties (width, orientation, etc.). This is discussed in detail in [28]. The mechanism of vortex motion can also be visualized. For instance, low-temperature SEM experiments or magneto-optic recording of flux motion and penetration demonstrates the presence of channels along which vortices preferentially move (Fig. 2.6).

2.3 Vortex Manipulation in HTS Films

The *flux-line shear* mechanism automatically affects the conditions for vortex manipulation in HTS. In contrast to the *collective pinning* mechanism that is demonstrated for weak-pinning superconductors (e.g. amorphous conventional superconductors such as a-Nb_xGe, a-Mo_xSi or a-Pb), the properties of weak-pinning channels determine vortex motion and, thus, generation of flux noise in HTS devices. Vortex pinning and motion in HTS films are defined by the film's inhomogeneity and the vortex–vortex interaction. Additional (artificial) pinning sites are not expected to have a large impact on the critical properties of these materials. As a consequence, the strategy for vortex manipulation has to be different compared to vortex manipulation in weak pinning (e.g. amorphous) superconductors.

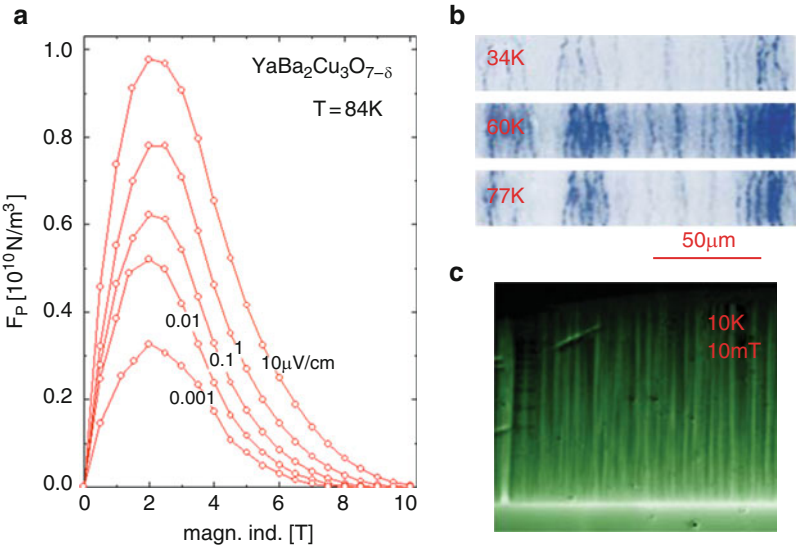

Fig. 2.6 Electronic and visual demonstration of the flux-line shear mechanism in high-T_c films: (**a**) magnetic field dependence of the volume pinning force for a YBCO thin film stripline at 84 K for various voltage criteria [28]; (**b**) low-temperature scanning electron microscope (LTSEM) voltage image of vortex motion in a 40-μm-wide YBCO stripline at various temperatures (R. Gross and D. Koelle, private communication) [29]; (**c**) Magneto-optical image of the flux distribution in a YBCO film on a 14° miscut $NdGaO_3$ substrate taken at 10 K and 10 mT. [12]. Darker areas correspond to larger contributions to flux motion (**b**) or smaller magnetic fields (**c**)

As a consequence, vortex manipulation has to be achieved via *guidance of vortices* rather than by vortex pinning or trapping for HTS films. The guidance of vortices could lead to a reduction in the driving force (e.g. guidance under an angle with respect to the Lorentz force, Sect. 2.3.3.2), guidance towards extended pinning centres (Sect. 2.3.3.1), guidance along special paths that reduce the impact of the motion of vortices (see for instance noise reduction in SQUIDs, Sect. 2.4.1), or guidance of vortices with asymmetric driving potential (see for instance vortex ratchets, Sect. 2.4.2.2). The different types of defects for guidance of vortices and the different strategies are sketched in the following sections.

2.3.1 Vortex Manipulation via Artificial Structures

Vortices can be manipulated by various modifications in the superconducting film.

1. Connected superconducting areas with locally tailored electrical properties (mainly "channels for vortex motion") are mainly aiming at vortex guidance. They can be created among others by:

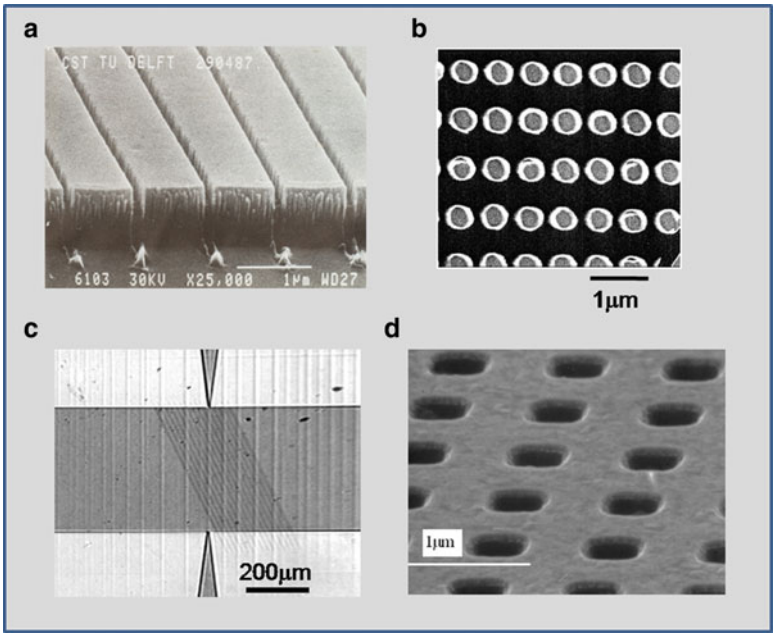

Fig. 2.7 SEM images of artificial structures for vortex guidance in NbN/Nb_3Ge bilayer [10,13,25] (**a**), magnetic dots (Ni) on Nb [30] (**b**), heavy-ion patterned channels in $YBa_2Cu_3O_{7-\delta}$ [31] (**c**) and antidots in $YBa_2Cu_3O_{7-\delta}$ [15,32,33] (**d**)

(a) Combination of weak and strong pinning material (Fig. 2.7a) [10, 13, 25]
(b) Thickness variation (see for instance [11])
(c) Grain boundaries and other extended natural defects (e.g. films on vicinal cut substrates, Fig. 2.6c) [12, 34]
(d) Modification of superconducting properties (e.g. ion beam patterning, Fig. 2.7c) [31]

2. Non-simply connected micro- or nanostructures will cause a long-range electronic or magnetic interaction between vortex and artificial structures. Arrangements (rows or arrays) of various structures are feasible and will lead to vortex pinning or trapping as well as vortex guidance. Different micro- and nano-objects are feasible:

(a) Dots (magnetic or non-magnetic) [30, 35–37]
(b) Completely etched holes (antidots) [14, 15, 32, 33, 38–43]
(c) Partially etched holes (blind holes) [44].

Not all of these structures are suitable for HTS films. Some of the different ways to control vortex pinning and vortex motion are sketched below.

Artificial channels: An obvious method to provide controlled vortex motion (guided vortex motion) is given by the pattering of narrow channels into

superconducting material. This can be done by etching channel structures into a single layer leading to modification of the pinning force due to thickness variation, local modification of the superconducting properties or by combining two layers of superconducting material with different pinning properties.

An intriguing example of easy vortex flow channels consists of a weak-pinning amorphous Nb_3Ge bottom layer combined with a strong-pinning NbN top layer, into which the small channels are etched (Fig. 2.7a). A detailed report of experimental results obtained from resistive measurements on these channels is given in [25], and simulation of the vortex motion in the channels is given in [13]. The vortices in the channels predominantly experience the interaction with the row of pinned vortices at the edge of the channel within the NbN. The commensurability between the vortex lattice with field dependent lattice parameter $a_o = b_o(\phi_o/B)^{1/2}$ and the channel size leads to periodic oscillations of the volume pinning force. It is demonstrated that vortices move within the channels if the total driving force on the vortices in the channel exceeds the shear forces at the channel edges.

Similar structures are possible for combinations of HTS films with weak pinning conventional superconductors. However, to preserve the high temperature operation, all high-T_c combinations have to be chosen. Since combinations of different HTS films prove to be difficult to obtain, modification of the superconducting properties are the easiest way to pattern channels into HTS films.

Heavy ion lithography: Ion irradiation of HTS films offers a unique possibility to create a wide range of different defects and to tailor the electrical and superconducting properties. Depending on the species of ions used during the irradiation, their energy and fluence, nanoscale columnar pinning centres can be created, which locally enhance or diminish the pinning properties. A review of this effect is given in this book [45]. While, the irradiation with relatively low fluence of high energy heavy ions leads to an enhancement of the critical current due to the strong vortex pinning at columnar defects, relatively high fluence leads to a reduction of the critical properties. Thus, the superconducting properties can be controlled and modulated locally. Recently, the preparation of artificial channels for flux motion has been demonstrated with this technology [31].

Dots and antidots: In contrast to simply connected structures, dots and holes (antidots) offer a number of advantages for the manipulation of vortices:

1. Dots and/or antidots of various size, properties and shapes can be used or even combined (see Sect. 2.3.3)
2. They can be positioned more or less at wish, fancy structures are possible (see Sect. 2.4.2.2)
3. They can be used as pinning or trapping sites as well as for guidance of flux
4. The superconductivity is not modified over the entire cross-section like in case of the formation of channels in HTS films

The latter is important for a number of possible applications, e.g. when a reduction in the transition temperature is not tolerable.

While (magnetic) dots have not been successfully been tested for HTS films, the preparation (of arrays) of micron- or nanosize antidots has been proven to be a very

effective way to manipulate flux in HTS films and devices. In contrast to other pinning defects, which have to be of the size of the superconducting coherence length ξ (core interaction [33, 46–51]), antidots with sizes much larger than ξ will trap magnetic flux very effectively [15]. The advances in lithography techniques and the possible use of antidots in applications (e.g. SQUIDs [52,53], vortex diodes [33,48–51] and microwave devices [57]) have led to a renewed interest in the research of superconducting films containing antidots or antidot lattices. Antidots are successfully prepared in films of conventional superconductors (typically weak pinning Pb, V, or a-WGe thin films, Pb/Ge multilayers, Pb/Cu bilayers or Nb foils) [14, 33, 39–41, 43, 58–63] as well as HTS material (YBCO) [15, 32, 33, 52, 53, 64]. Intensive studies have been performed of:

1. Commensurability effects (matching effects) between the antidot lattice and vortex lattice
2. Multiquanta formation in the antidots
3. Guided motion along rows of antidots (e.g. via resistive Hall-type measurements)
4. Visualization of vortex motion (e.g. magneto-optical imaging, Hall-probe scanning microscopy, Lorentz microscopy)
5. Implementation of antidots in cryoelectronic devices (e.g. noise reduction in SQUIDs or improvement of the microwave properties of HTS resonators and filters)

2.3.2 *Theoretical Considerations of Vortex Manipulation via Antidots*

There are a number of theoretical methods to analyse vortex matter in patterned superconducting thin films ranging from electrodynamics, free energy considerations and Ginzburg–Landau formalism to numerical computer simulation. A few basic ideas are sketched in this section.

Computer simulations of vortex motion in thin films are usually based on 1D or 2D (depending on the examined problem) versions of a molecular dynamics code solving the overdamped equation of motion for individual vortices that are subject to an external driving force (e.g. Lorentz force f_L), vortex–vortex repulsion f_{VV} and additional forces (e.g. due to thermal fluctuations f_T). The net force f_i acting on an individual vortex and that leads to a motion with velocity v_i that is typically given by [46, 65–68]:

$$\vec{f}_i = \vec{f}_L + \vec{f}_{VV}(\vec{r}_i) + \vec{f}_p(\vec{r}_i) + \vec{f}_T(\vec{r}_i) = \eta\vec{v}_i. \tag{2.13}$$

With adequate expressions for the different forces and the viscosity η molecular dynamics simulation of vortex motion has proven to be a powerful tool for analysing, predicting and visualizing vortex dynamics in complex thin film systems including studies of vortex phases and phase transitions, vortex mobility and

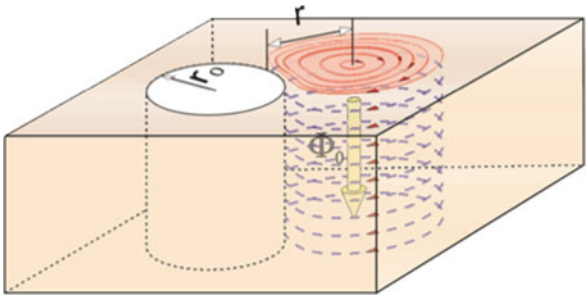

Fig. 2.8 Sketch of a vortex interacting with a cylindrical cavity (e.g. an antidot with radius r_o) [54]

dynamics up to the development of novel "fluxonic" devices. The major handicap of this approach is given by the fact that vortices are treated as "molecules" in this model, i.e. modifications of vortices for instance at boundaries – especially, vortex nucleation or annihilation – are not properly described (Fig. 2.8). The latter is of importance for the description of vortex mater in micro- or nanostructured superconductors.

Vortex–antidot interaction: The interaction energy between a vortex and a small insulating cylindrical cavity (analogue to an antidot) in high-κ superconductors has been calculated using the London approximation [55] and in an alternative approach (using the analogy between a vortex close to an antidot and a charge line in an infinite dielectric close to a cylindrical cavity of different dielectric permittivity) in [56]. Later, the calculations have been extended to arbitrarily large cavities [69]. It is demonstrated that the interaction energy becomes the same as the one between a vortex and the straight edge of a superconductor (Bean–Livingston barrier [70]) when the radius of the antidot goes to infinity. Although the precise form of the interaction potential between a vortex and a cylindrical antidot is slightly different in these studies [55, 56, 69], the main conclusions are identical.

Based on a series expansion of Bessel functions K_o of the second kind, the free energy of a vortex at a radial distance r of an antidot with radius r_o is given by [55, 56]:

$$F(r) = \frac{\Phi_o^2}{4\pi\mu_o\lambda^2}\left[K_o\left(\frac{\xi}{\lambda}\right) + n^2 K_o\left(\frac{r_o}{\lambda}\right) + 2nK_0\left(\frac{r}{\lambda}\right) + \ln\left(1 - \frac{r_o^2}{r^2}\right)\right] \quad (2.14)$$

for $\xi < (r,\ r_o) << \lambda$ and n representing the number of flux quanta that are already trapped in the antidot. The elementary vortex–antidot interaction is given by $f_{VA} = -\partial F/\partial r$.

The vortex–antidot interaction depends upon the magnetic flux $\Phi = n\Phi_o$ trapped in the antidot (Fig. 2.9). The interaction between a vortex and an "empty" antidot is attractive for all vortex–antidot distances. As soon as one flux quantum is trapped in the antidot, the interaction potential changes and a surface barrier emerges at the edge of the antidot. The height of the barrier increases with increasing number of

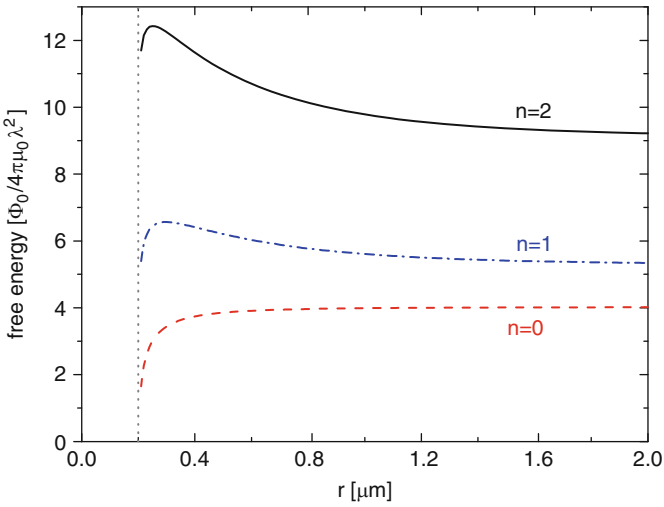

Fig. 2.9 Free energy of a vortex as function of the radial distance from an antidot for different occupation numbers n of the antidot with $\lambda = 600\,\text{nm}$, $\kappa = 50$ and $r_o = 200\,\text{nm}$

trapped flux quanta. This automatically defines a saturation number n_s. For $n \geq n_s$, the interaction becomes repulsive, and no additional flux can be trapped by the antidot. The saturation number depends upon the size of the antidot. For small antidots (single antidot with $r_o \ll \lambda$), the saturation number can be approximated by [55]

$$n_s \cong \frac{r_o}{2\xi(T)}. \tag{2.15}$$

The pinning force per unit length depends on the radial distance between vortex and antidot and has a maximum value close to the antidot edge:

$$f_{p,max} \approx \frac{\Phi_o^2}{4\sqrt{2}\pi\mu_o\lambda^2\xi}\left(1 - \frac{n}{n_s}\right), \tag{2.16}$$

i.e. the maximum vortex–antidot interaction decreases with increasing occupation number and becomes zero for $n = n_s$.

Generally, the saturation number depends upon temperature, i.e. it increases with decreasing temperature. Furthermore, a consequence of a saturation number $n_s > 1$ is the formation of so-called multi-quanta vortices. Experimental proofs of the existence of multi-quanta vortices will be given in Sect. 2.3.3.1.

Ginzburg–Landau formalism: Vortex matter in nanostructured superconductors is generally very complicated. For instance, flux motion across a superconducting microbridge (e.g. formed by closely spaced antidots) of the size of the characteristic length of the superconductor will not lead to vortex formation. A phase slip line will develop along the path of the flux motion leading to Josephson-like behaviour of the

bridge [71]. According to theory, the characteristic length of the superconductor for this effect should be the coherence length ξ. However, it has been shown that phase slip lines are present for bridge dimensions w up to the penetration length λ [71]. The effective penetration length $\lambda_{\mathrm{eff}}(T) = \lambda_{\mathrm{L}}(T)\mathrm{coth}[d/2\lambda_{\mathrm{L}}(\mathrm{T})]$ in thin $YBa_2Cu_3O_{7-\delta}$ films with thickness of typically $d = 80$–200 nm range between 400 and 1000 nm. Furthermore, it has been shown that phase slip can be present even in bridges with larger dimensions, i.e. up to $w = 1$–$1.5\,\mu\mathrm{m} > \lambda$ [72, 73].

Another interesting effect that might be relevant for the nucleation of vortices in mesoscopic systems is known from observations of classical von Karman vortices. After nucleation the vortex structure develops in time. Due to the motion, a given space is necessary for a vortex to fully develop. If this space is not provided, vortices will not be originated. A similar situation might apply for Abrikosov vortices in mesoscopic superconductors. The nucleation of flux in the superconductor and its shuttling between adjacent antidots might not lead to vortex formation due to the restricted distance between the antidots. This is among others described by the term "kinematic" vortices [74].

As a consequence, flux transport in HTS microstructures (e.g. closely spaced antidots) is not properly described by molecular dynamics or energy considerations that are based on "pristine" Abrikosov vortices. For this problem, the Ginzburg–Landau formalism might be more adequate.

Depending on the considered problem, different approaches are chosen. In the *stationary case*, a self-consistent set of differential equations has to be solved for the order parameter ψ and the vector potential $\mathbf{A}$ of a magnetic field $\mathbf{H} = \nabla \times \mathbf{A}$ [75, 76] which can be presented in the dimensionless form as follows:

$$\begin{aligned} &(-i\nabla - \mathbf{A})^2\psi - \psi\left[\left(1 - \tfrac{T}{T_c}\right) - |\psi|^2\right] = 0 \\ &-\kappa^2\Delta\mathbf{A} = -\tfrac{i}{2}(\psi * \nabla\psi - \psi\nabla\psi *) + \mathbf{A}\,|\psi|^2 = \mathbf{j}, \end{aligned} \tag{2.17}$$

with the boundary condition $\mathrm{n}(-i\nabla\psi - \mathbf{A}\psi)|_{\mathrm{boundary}} = 0$, $\mathbf{n}$ representing the unit vector normal to the boundary and $\kappa = \lambda(T)/\xi(T)$. For the analysis of *dynamic problems*, the time-dependent Ginzburg–Landau equation has to be used [77–79] where the time τ_{in} of the nonequilibrium quasiparticle distribution function is explicitly included.

Solutions based on the Ginzburg–Landau formalism exist among others for the vortex–antidot interaction [54], the current and magnetic field distribution in nanostructured films (e.g. for superconducting films with antidot arrays Fig. 2.10), the vortex and flux transfer between antidots (e.g. see Fig. 2.11) and the vortex dynamics up to high velocities [81].

Critical vortex velocity: Studies of the energy dissipation due to vortex motion is predominantly focussed on the limit of small driving forces and small frequencies, i.e. the onset of vortex dynamics in the limit of small vortex velocities. However, a number of HTS applications such as coated conductors, fault-current limiters or microwave devices operate at high power levels or frequencies and, therefore, potentially in the regime of high vortex velocities. Based on Eliashberg's

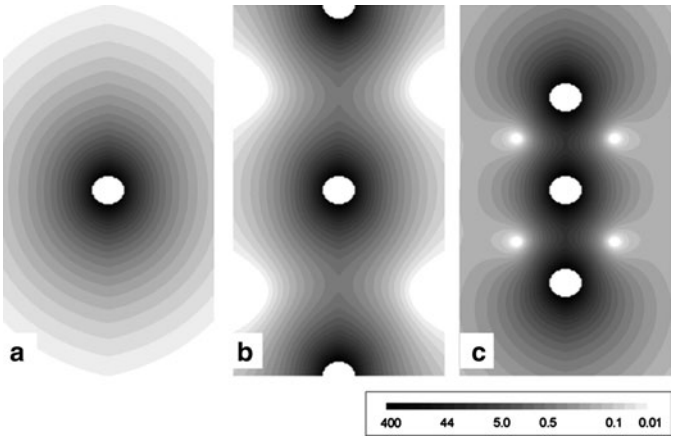

Fig. 2.10 Density distribution of the screening current for two-dimensional superconductor (e.g. thin film) with a row of antidots placed at different distances d_v (measured in units of the antidot radius) from each other obtained from simulations on the basis of the Ginzburg–Landau equations in the high-κ limit: (**a**) $d_v = 66.7$, (**b**) $d_v = 13.3$, (**c**) $d_v = 6.7$. High local current densities are indicated with dark grey; the scale is given in arbitrary units [33]

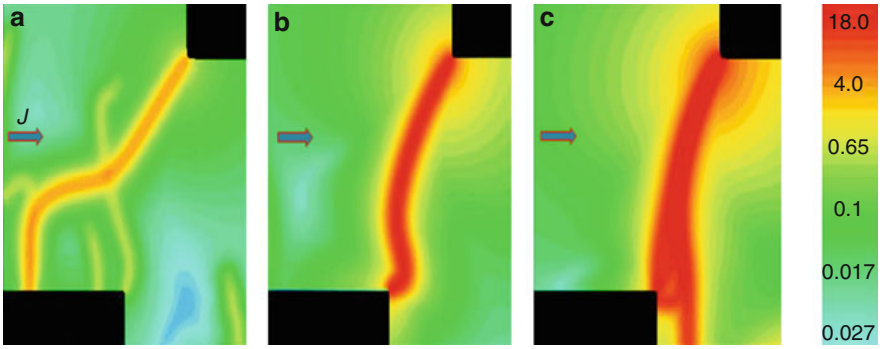

Fig. 2.11 Accumulated trajectories of vortices in a thin YBCO film with two indentations (antidots) for different applied current densities $0.333 \times 10^{10}\,\mathrm{A/m^2}$ (**a**), $0.666 \times 10^{10}\,\mathrm{A/m^2}$ (**b**) and $1.332 \times 10^{10}\,\mathrm{A/m^2}$ (**c**). The sizes of the areas are $0.24\,\mu\mathrm{m} \times 0.24\,\mu\mathrm{m}$, the *black* areas represent parts of the square size antidots and the *arrow* indicates the nominal direction of the applied current [80]

ideas on non-equilibrium effects in superconductors, Larkin and Ovchinnikov predicted that a non-equilibrium distribution and relaxation rate of the normal charge carriers (treated as quasiparticles) develop during the motion of vortices at high velocities [82]. As a result, they expected a discontinuity in the current–voltage characteristic (IVC).

According to the Larkin and Ovchinnikov (LO) theory, the viscous damping coefficient at a vortex velocity v is given by [82]:

$$\eta(v) = \eta(0)\left[1 + \left(\frac{v}{v^*}\right)^2\right]^{-1}, \tag{2.18}$$

with a critical vortex-velocity v^*:

$$v^* = \left[\frac{D\sqrt{14\zeta(3)}}{\pi\tau_{\mathrm{in}}}\sqrt{1 - \frac{T}{T_{\mathrm{c}}}}\right]^{1/2}, \tag{2.19}$$

τ_{in} denoting the inelastic quasiparticle scattering time, $\zeta(x)$ the Riemann–Zeta function, $D = v_{\mathrm{F}} l_{\mathrm{o}}/3$ the quasiparticle diffusion coefficient, v_{F} the Fermi velocity and l_{o} the electron mean free path. According to LO, a nonlinear IVC is expected for a critical electric field $E^* = v^* B$ according to:

$$J = \frac{E}{\rho_{\mathrm{ff}}}\left\{\left[1 + \left(\frac{E}{E^*}\right)^2\right]^{-1} + \gamma\left[1 - \frac{T}{T_{\mathrm{c}}}\right]^{1/2}\right\} + J_{\mathrm{c}} \tag{2.20}$$

with $\gamma \approx 1$. This behaviour (see sketch in Fig. 2.12a) is observed for conventional superconductors [85, 86] as well as for high-T_{c} thin films [83, 84, 87]. It appears for instance when the current limit is exceeded in superconducting resistive fault-current limiters. In this case, the limiter shows an extremely sharp and sudden voltage peak at the critical electric field E^* during the quench of the superconductor at high power [88].

Large vortex velocities are also expected in fluxon devices working at high frequencies. For instance, a net flux transport in an impedance-matched microwave stripline would require a vortex motion across in a stripline of a typical width of $w = 400$–$500\,\mu\mathrm{m}$ in a time $t < 1/2f$. As a result, a vortex velocity $v > 1\,\mathrm{km/s}$ is expected for frequencies $f > 1\,\mathrm{MHz}$. Thus, vortex velocities that clearly exceed the critical velocity for high-T_{c} films are expected for fluxon devices operating in the MHz–GHz frequency regime and temperatures not too close to T_{c} (see inset of Fig. 2.12b). One of the major questions is whether vortex properties such as vortex–antidot interaction or vortex mobility will be modified at high frequencies.

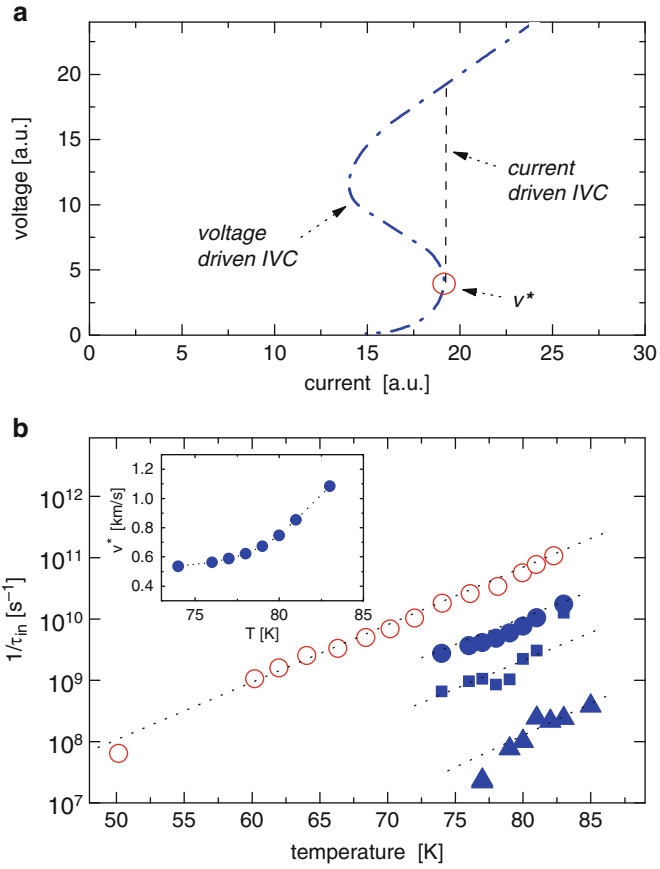

Fig. 2.12 (**a**) Schematic drawing of voltage-controlled and current-controlled IVCs measured up to voltages $V > V^*$ and (**b**) inelastic scattering rate and critical vortex velocity (*inset*) as function of temperature for YBCO films obtained from IVC measurements via rapid current ramps (*open symbol*) [83] and current pulses (*solid symbols*) [84]

2.3.3 Experimental Demonstration

Vortex manipulation has been demonstrated among others via microscopy (scanning Hall experiments, magneto-optic imaging, Lorentz microscopy or laser scanning microscopy), resistive, Hall-type, inductive or magnetization measurements or microwave experiments. Most of these experiments have been performed for weak pinning superconducting systems (e.g. Pb, V, or a-WGe thin films, Pb/Ge multilayers, Pb/Cu or Nb/Ni bilayers). However, for most applications strong-pinning superconductors and, especially, high-T_c films are of interest.

A first report of a successful preparation and a clear indication of an attractive interaction between antidots and vortices in HTS is given in [15]. Based on

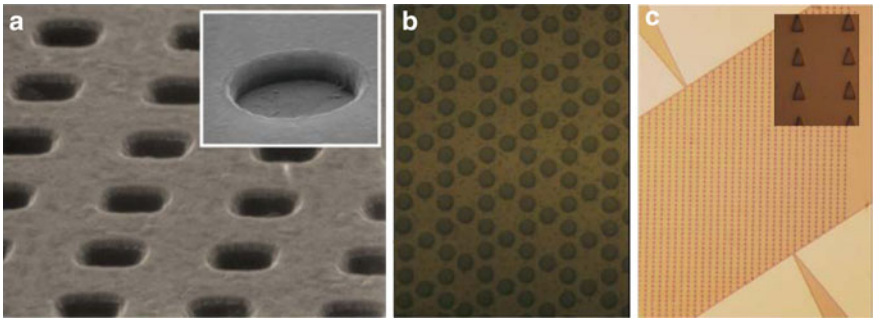

Fig. 2.13 SEM images of various antidot lattices in YBCO films: (**a**) square lattice (periodicity $d_{AA} = 1\,\mu m$, antidot radius $r_o = 220\,nm$), (**b**) Kagome lattice ($d_{AA} = 6\,\mu m$, $r_o = 1\,\mu m$), and (**c**) rows of anisotropic antidots ($d_{AA} = 10\,\mu m$ in the row)

this work, antidots in HTS thin films have been used for guidance of vortices, microwave experiments, improvement of existing HTS devices and development of novel fluxon concepts.

Generally, high structural perfection and small surface roughness are required for an optimized patterning process for micrometer and, especially, for submicrometer structures in YBCO films. Furthermore, for microwave experiments suitable substrates (e.g. $LaAlO_3$ or CeO_2 buffered sapphire) should be chosen. High quality $YBa_2Cu_3O_{7-\delta}$ (YBCO) films are typically deposited via PVD technologies, e.g. high-pressure sputter technique, pulsed laser deposition or thermal coevaporation. Typical deposition parameters are for instance:

- *Pulsed laser deposition*: substrate temperature of 700 °C, pressure of 0.5 mbar of pure oxygen, pulse rate of 10 Hz (1 J/pulse) and energy density of $5\,J/cm^2$ at the target lead to a deposition rate of $\sim 1.67\,nm/s$
- *Sputter deposition*: 6″ dc magnetron at 180 W, pressure of 0.6 mbar of Ar/O_2 ratio of 2:1, heater temperature of 870 °C yield a deposition rate of $\sim 0.8\,nm/min$ for YBCO and 6″ rf magnetron at 150 W, 0.13 mbar of Ar/O_2 ratio of 8:1, heater temperature of 870 °C yield a deposition rate of $\sim 0.3\,nm/min$ for CeO_2.

Typical images of antidots and antidot lattices in YBCO films are given in Fig. 2.13. In the following sections, experimental results are discussed that are recently obtained for vortex manipulation via antidots in high-T_c films.

2.3.3.1 Vortex–Antidot Interaction and Multi-Quanta Formation

First clear indications of an attractive interaction between antidots and vortices in HTS are given in [15]. Figure 2.14 represents a comparison between the magnetic field dependence of critical current I_c and critical current density J_c as a function of the magnetic field for a YBCO thin films with and without antidots. First, the critical current seems to be enhanced by the presence of the antidot lattice (inset

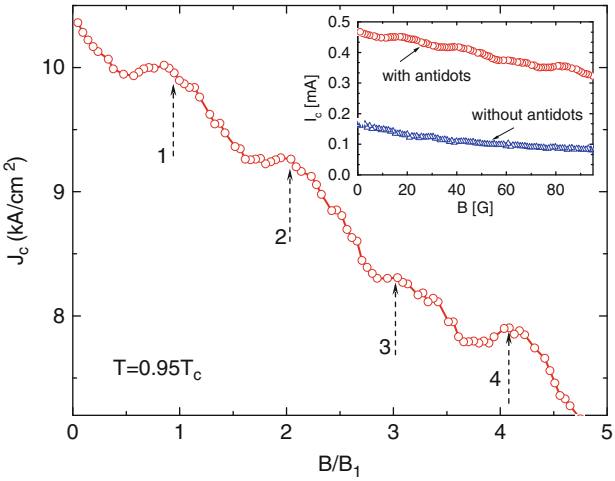

Fig. 2.14 Critical current density and critical current (*inset*) as a function of magnetic induction for YBCO without and with antidots measured at $T = 0.95\ T_c$ [15]. The antidot lattice is shown in Fig. 2.13a; it is a square lattice with periodicity $d_{AA} = 1\,\mu$m and antidot radius $r_o = 220$ nm. The resulting first matching is expected to be $B_1 = \Phi_o/d_{AA}^2 = 2.07$ mT. Both samples (with and without antidots) are obtained from the same film and posses identical dimensions

of Fig. 2.14). It demonstrates the additional flux pinning provided by the antidots. Second, the reference sample (patterned simultaneously into the same film but without antidots) shows the usually observed monotonic field dependence of J_c. In contrast, the perforated YBCO stripline shows peaks or cusps in the magnetic field dependence of the critical current at the theoretically expected matching fields $B_n = nB_1$. Matching peaks could be resolved at integer $n = 1, 2, 3$ and 4. In Sect. 2.4.1.1, it is shown that commensurability effects are even present at rational positions (n/m [89]). Small shifts in the peak positions have to be ascribed to field gradients in the sample that develop during the field ramps in strong-pinning material [15]. The experiments shown in Fig. 2.14 are executed at temperatures close to T_c. The enhancement of the volume pinning force and the presence of matching effects [cusps in $J_c(B)$] could be resolved only down to temperatures of about 50 K. At lower temperatures, the pinning by natural defects seems to dominate the vortex–antidot interaction.

Another interesting aspect of vortex pinning by antidots is given by the formation of *multi-quanta vortices*. Already in the first theoretical considerations [55] a flux occupation of the antidot of $\Phi = n\Phi_o$ with $1 \leq n \leq n_s$ [see (2.15)] was predicted. Due to their specific character, antidots trap quantized flux and not Abrikosov vortices. By producing the so-called blind holes (not completely etched holes), the Abrikosov vortex character is preserved and the formation of multi-flux-quanta trapping by antidots can be visualized in the form of flux splitting into single-flux-quanta vortices within each blind hole. This phenomenon has been demonstrated

via Bitter-decoration experiments on Nb films with regular arrays of blind holes [60, 61].

The existence of multi-quanta vortices in antidots in HTS thin films has been demonstrated by inductive measurements that have been performed on YBCO films with regular square lattices of antidots (Fig. 2.15) [32]. The experimental technique is based on the superposition of an ac and dc magnetic field normal to the film surface. The amplitude of the ac field is typically much smaller than the amplitude of the dc field. The in-phase and out-of-phase components of the fundamental signal are recorded by the pick-up coil. They are proportional to the in-phase and out-of-phase components of the complex susceptibility $\chi(T, B) = \chi'(T, B) + i\chi''(T, B)$ that represent the stored energy ($W_m = \chi' {B_a}^2/2\mu_o$) and the

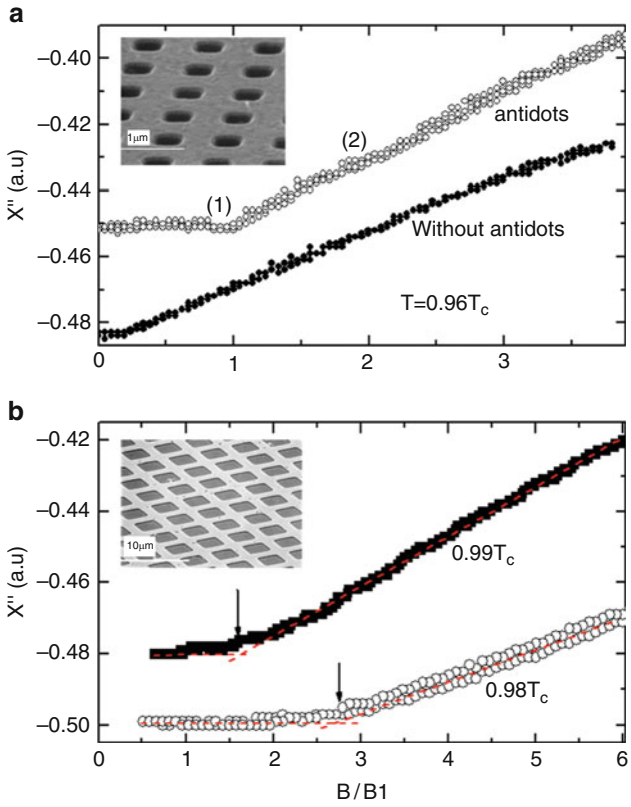

Fig. 2.15 Out-of-phase susceptibility component χ'' as a function of the dc bias field for YBCO films without and with a square lattice of antidots of different sizes [32]. B_1 refers to the first matching field of the given antidot lattice. (**a**) χ'' obtained for a reference film (without antidots) and a film with an antidot lattice ($d_{AA} = 1\,\mu m$, antidot radius $r_o \approx 0.34\,\mu m$) at $T/T_c = 0.96$ ($n_s = 1$). (**b**) χ'' is shown for a film with an antidot lattice ($d_{AA} = 5\,\mu m$, $r_o \approx 1.75\,\mu m$) at $T/T_c = 0.99$ ($n_s \approx 2$) and $T/T_c = 0.98$ ($n_s \approx 3$). The insets show SEM images of the YBCO films with different square lattices

dissipated energy ($W_q = 2\pi\chi''$), respectively. By varying the dc magnetic field B, the dissipated energy due to vortex motion in the film can be recorded as a function of temperature and field.

Figure 2.15 shows the variation of out-of-phase component χ'' as a function of the magnetic field at temperatures close to T_c (high mobility of the vortices) for YBCO thin films without antidots and with square arrays of antidots of different sizes. For the measurements on the reference films without antidots, χ'' increases monotonically (except for the fields below the magnet's remnant field of about 0.5 mT). In contrast, the out-of-phase component for the film with small antidots is constant up to the first matching field B_1 for which the density of vortices matches the density of antidots. Above B_1, χ'' increases with a slope similar to that observed for the reference sample. Small curvatures are observed at the matching fields $2B_1$ and $3B_1$. The inductive measurement of the antidot sample in Fig. 2.15a confirms the presence of matching effects and demonstrates that the saturation number $n_s = 1$ for this antidot configuration and temperature. Multi-quanta vortices are expected at lower temperatures. Unfortunately a high mobility of the vortices is needed for this experiment; hence, experiments at lower temperatures are not possible. However, by increasing the size of the antidots the presence of multi-quanta vortices can be demonstrated. This is demonstrated in Fig. 2.15b for larger antidots ($r_o \approx 1.75\,\mu m$) where the saturation number n_s changes from 2 to 3 for a small temperature reduction.

Multi-quanta formation in antidot arrays in YBCO films has also been visualized via high-resolution magneto-optic technique that produces a 2D image of the local magnetic field [90, 91]. Figure 2.16 shows a 3D reconstruction of the trapped flux in a hexagonal antidot lattice in a YBCO film, which was recorded at 7 K and zero magnetic field after a field of $B = 1$T had been removed. The height of the peaks

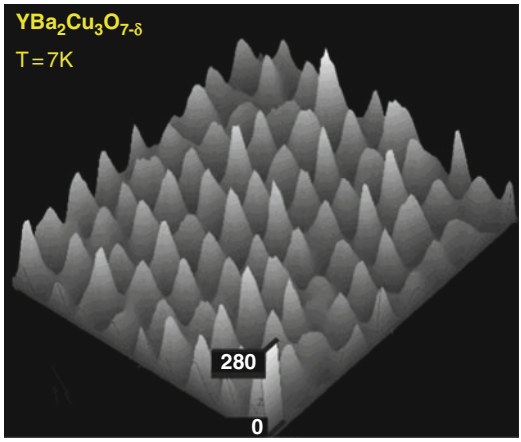

Fig. 2.16 Reconstruction of the trapped magnetic flux distribution obtained from a magneto-optic image that was recorded at 7 K in zero-field after applying at field of 1T [90]. The local field shows clear maxima at the position of the antidots (*triangular lattice*, $d_{AA} = 10\,\mu m$, $r_o \approx 1\,\mu m$). The scale for the height of the peaks is given in numbers of trapped flux quanta

represents the amount of trapped flux quanta. No flux (vortices) could be detected between the antidots which indicate the higher mobility (small pinning potential) of the interstitial vortices compared to flux in the antidots. Multi-quanta vortices with flux up to $\Phi = 280\ \Phi_o$ are trapped at this temperatures after removal of the field. Inserting $n_s \approx 280$ into expression (2.15) yields a reasonable value for the coherence length, i.e. $\xi(7\text{K}) \approx 1.8$ nm. Furthermore, using the extended expressions [92] derived for the saturation number in square or hexagonal arrays leads to a reasonable value for the lower critical field of $B_{c1}(7\text{K}) \approx 41$ mT [15].

2.3.3.2 Guided Vortex Motion via Antidots

Probably even more important than flux trapping is the guidance of vortices by artificial defects for the general understanding of vortex matter and applications of HTS. Guided motion has been demonstrated in conventional weak pinning superconductors using lithographically etched channels (Fig. 2.7a) [10, 13, 25]. The use of connected superconducting areas with locally tailored electrical properties that form channels for flux motion is also possible for HTS material. Guidance has been demonstrated with channels prepared by heavy ion irradiation [31] in HTS thin films. However, an intriguing and more flexible method of vortex guidance is provided by special arrangements of antidots [90, 91].

First indications for guidance of vortices by rows of antidots have been obtained from magneto-optic imaging of flux penetration in patterned HTS films [91]. Figure 2.17 represents a magnetic-field map of a disc-shaped YBCO thin film after cooling in zero field to 4.2 K and successive increase in the field up to 30 mT. There are two important features [91]:

1. The flux penetration pattern shows a very clear fourfold (D_4) symmetry, i.e. the penetration is highly anisotropic, compared to the cylindrical symmetry that is observed for non-perforated disc samples.
2. The flux penetrates preferentially along the antidot lattice vector that is closest to the direction of the Lorentz force. The Lorentz force is caused by the screening current, and its direction is normal to the edge of the sample.

A first basic explanation of the angular dependence of the guidance of vortices via rows of antidots is given by the n-channel model [33]. The sketch in Fig. 2.18 illustrates the angular dependence of V_{Hall} given in a simplified one-channel model, in which the flux is expected to drift only along rows of antidots. The orientation of the rows is given by the angle γ. The component of the Lorentz force, which compels vortices to move along the antidot rows (i.e. guided motion), is $F_{\text{guid}} = F_{\text{L}} \cos\gamma$, where F_{L} is the modulus of the Lorentz force: $F_{\text{L}} = |\boldsymbol{F}_{\text{L}}|$. The components parallel and perpendicular to the applied current are:

$$\begin{aligned} F_{\text{x,guid}} &= F_{\text{guid}} \sin\gamma = F_{\text{L}} \cos\gamma \sin\gamma \\ F_{\text{y,guid}} &= F_{\text{guid}} \cos\gamma = F_{\text{L}} \cos^2\gamma, \end{aligned} \tag{2.21}$$

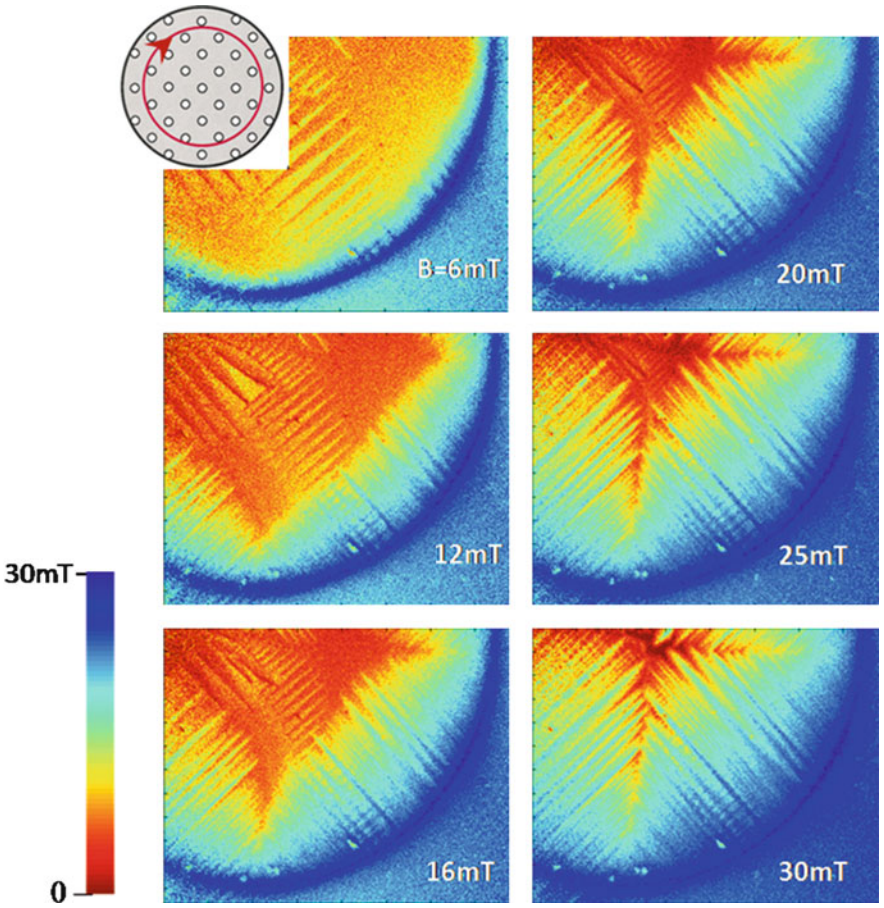

Fig. 2.17 Magneto-optic visualization of the anisotropic (guided) flux penetration in a disk-shaped YBCO film with a square lattice of antidots ($d_{AA} = 10\,\mu m$, $r_o \approx 1\,\mu m$) according to [91]. To enhance spatial resolution, only one-quarter of the disk is shown. The images are obtained at 4.2 K after zero field cooling, the field is gradually increased to $B_a = 6$, 12, 16, 20, 25 and 30 mT, respectively. The scale indicates the magnitude of the local field. The orientation of the square antidot lattice and the direction of the screening current that leads to radial oriented Lorentz force are indicated in the sketch

with $F_{x,guid}$ and $F_{y,guid}$ contributing to the Hall and longitudinal voltage signal, respectively. The experimentally determined angular dependence of the Hall voltage roughly obeys this simple relation $V_{Hall} \propto F_L \cos\gamma \sin\gamma$ obtained in this "1- channel model" [33]. Actually, it has to be considered that vortices can move with some probability also between antidots of neighbouring rows. These additional channels of vortex motion become important for large angles γ (Fig. 2.22) [93]. However, for these values of γ, the contribution of the vortex motion to V_{Hall} is small [see (2.21)]. Nevertheless, taking into account these additional channels of vortex

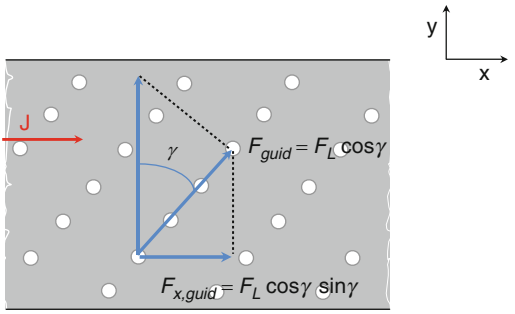

Fig. 2.18 Schematic illustration of the angular dependence of the Hall signal according to the n-channel model [33]

motion (i.e. vortices motion between antidots of adjacent rows) (2.21) should be substituted by a more general expression yielding

$$V_H \propto \sum_i P_i(\gamma) F_L \cos\gamma \ \sin\gamma, \tag{2.22}$$

where the summation is performed over all the channels of vortex motion, and $P_i(\gamma)$ is the angle-dependent probability of the motion along the i-th channel.

In order to obtain a more detailed insight into the guidance of vortices via rows of antidots, resistive six-probe dc measurements are executed on HTS films equipped with rows of antidots that simultaneously record the longitudinal voltage signal and the Hall signal [33,64]. Figure 2.19a shows schematically the typical sample design that is also suitable for microwave experiments on vortex manipulation [64].

The longitudinal voltage (contacts V_x) represents the standard parameter to characterize the critical properties of a superconducting stripline. In the normal regime, $V_{longitudinal}$ represents the normal state resistivity, whereas in superconducting regime it is generated by the component of vortex motion along the Lorentz force. In the latter case, $V_{longitudinal}$ is a measure for the flux transfer across the stripline that is collected between the longitudinal voltage contacts labelled V_x (integral signal). It characterizes the average velocity component $<v_y>$ of vortex in the stripline. In contrast, the Hall signal in superconducting regime characterizes the complementary velocity component $<v_x>$ of vortex and represents a more local analysis of the vortex motion that is restricted to the vicinity of the contacts pair (Hall contacts V_y in Fig. 2.19a).

High-T_c materials typically reveal the, so-called, anomalous Hall effect (AHE), i.e. the sign inversion of the Hall signal below T_c [94–103]. It has been shown that the AHE in high-T_c material is caused by vortex motion. Most likely the additional component of vortex motion is caused by the Magnus force affecting vortex motion close to T_c when pinning is very weak [103]. At temperatures close to T_c, the AHE competes with the guidance of vortices by rows of antidots [guided motion (GM)]. Depending on the orientation of the rows of antidots, the AHE will be suppressed. This is sketched in Fig. 2.19a for different orientations γ of rows of antidots. The experiment (Fig. 2.19c) shows the transition to the superconducting

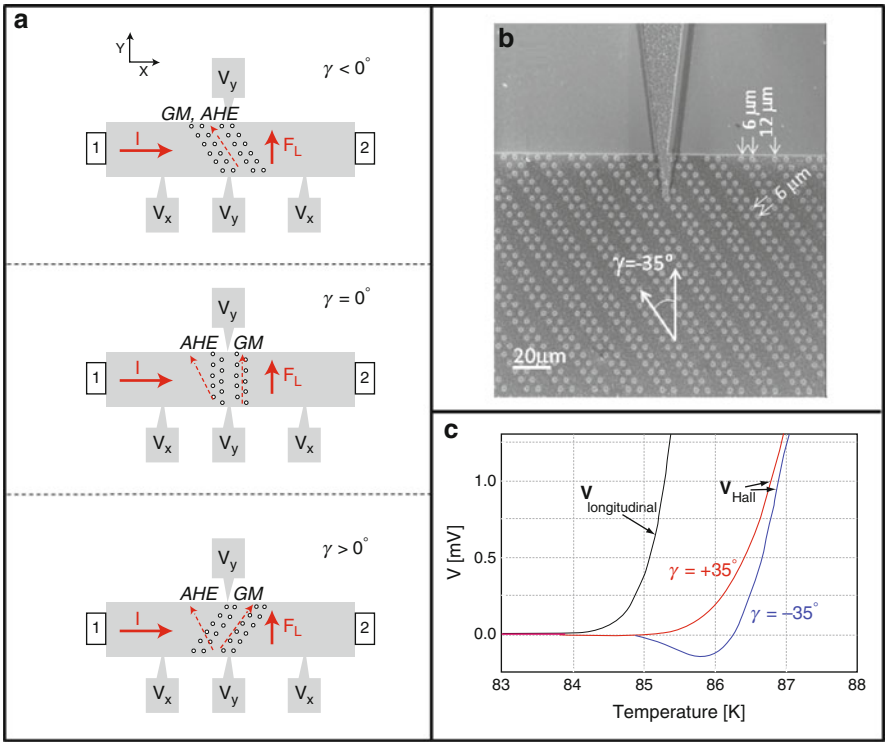

Fig. 2.19 (**a**) Sketch of a typical arrangement of antidots lattices for six-probe dc and microwave measurements of the longitudinal and Hall voltage to analyse guided vortex motion via rows of antidots and the anomalous Hall effect for negative, zero and positive angles γ, respectively. The angle γ is defined by the nominal direction of the Lorentz force due to the current and the orientation of the rows (single, pairs or triple rows are examined). The voltage probes, input and output ports for dc and microwave current (1, 2), the directions of current, Lorentz force, anomalous Hall effect (AHE) and guided motion (GM) are shown. (**b**) Microscopic image of a section of a sample depicting one of the Hall contacts and the configuration of antidot rows for $\gamma = -35°$. (**c**) Temperature dependence of the longitudinal voltage (contacts V_x) and Hall signals (contacts V_y) at the transition temperature. Depending on the direction of rows of antidots contacts, the anomalous Hall effect is present ($\gamma = -35°$) or suppressed ($\gamma = +35°$)

state determined by the measurements of the longitudinal voltage together with the temperature dependence of the Hall signals for two designs $\gamma > 0°$ and $\gamma < 0°$. While the Hall contacts positioned at antidots rows with $\gamma > 0°$ display the AHE, the Hall signal measured at antidots rows with orientation $\gamma < 0°$ do not show signs of an AHE.[1]

[1] Please note that the longitudinal voltage collects the total flux transport across the stripline registered between the voltage contacts V_x, whereas the Hall signal records the vortex motion "across the imaginary line between each pair of Hall contacts V_y". Consequently, the longitudinal voltage

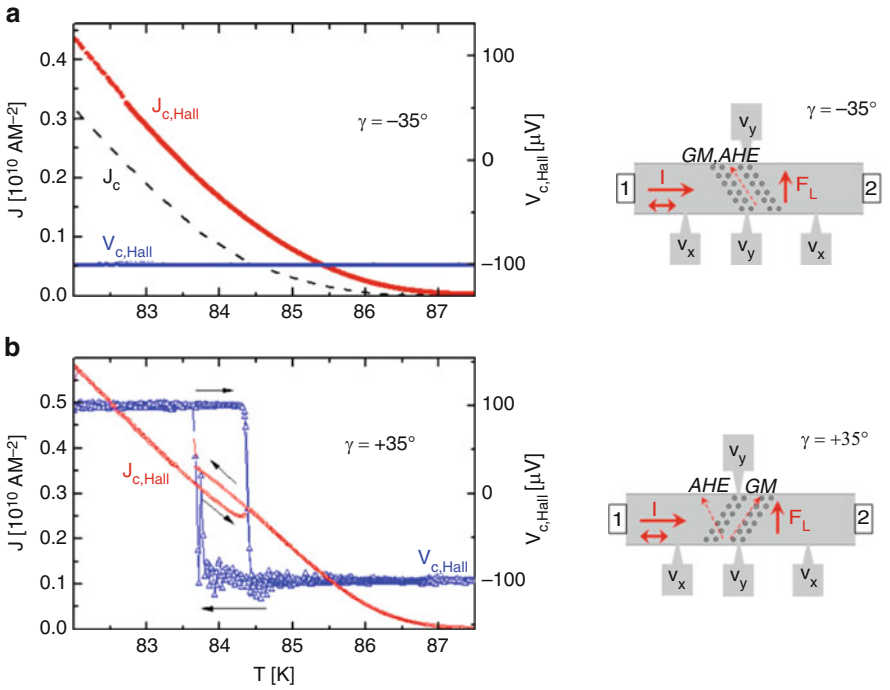

Fig. 2.20 Critical current densities $J_c(T)$ (*black dashed line*, voltage criterion $V_c = 5\,\mu V/cm$) and $J_{c,Hall}(T)$ (*red plot*) for two different orientations of rows: $\gamma = -35°$ (**a**) and $\gamma = +35°$ (**b**). $J_{c,Hall}$ is defined by a Hall voltage $|V_{c,Hall}| = 100\,\mu V$ (*blue line* and *triangles*). The *arrows* indicate the direction of temperature change during the experiment, and the magnetic field was 0.6 mT. *Right side*: the corresponding sample configurations from Fig. 2.19

Measurements of the transition curves (e.g. in Fig. 2.19c) are typically performed at small current densities. In the following, the impact of larger driving forces (i.e. large current densities) on the guidance by antidots is discussed. Additionally to the transition temperature, the critical current density J_c can be recorded via the different contacts. The standard J_c value is defined by measurements of the longitudinal voltage (voltage contacts V_x). It defines the onset of vortex motion and is determined by keeping the longitudinal voltage constant (typically at a value of a voltage criterion of a few $\mu V/cm$). The resulting current defines the critical current $I_c = J_c dw$ (d and w represent the thickness and width of the stripline). For YBCO films with and without antidot arrangements, $J_c(T)$ shows the classical behaviour, i.e. J_c decreases linearly with increasing temperature and at the transition this decrease smoothly approaches zero (Fig. 2.20a).

signal is orders of magnitudes larger compared to the Hall signal for the case of vortex motion. Therefore, a finite signal $V_{longitudinal}$ persists to lower temperatures where the Hall signal is already so small that it cannot be measured.

Similar to measurements of the classical critical current, we could keep the component of vortex motion $<v_x>$ constant by controlling the Hall signal. This way, the critical current density $J_{c,Hall}$ is defined in analogy to the classical critical current density J_c defined by the longitudinal voltage. The advantage of the analysis of $J_{c,Hall}$ is that a defined component of vortex motion perpendicular to the Lorentz force is established. This component of motion can only be caused by additional forces acting perpendicular to the Lorentz force, like the Magnus force or the guidance force. Therefore, $J_{c,Hall}$ is more suitable to characterize properties related to these forces than the classical definition of J_c.

Figure 2.20 shows the plots of critical current densities $J_{c,Hall}$ for both orientations of rows of antidots in a small applied magnetic field of 0.6 mT. To obtain a high mobility of vortices, a large voltage criterion is chosen for these measurements, $|V_{c,Hall}| = 100\,\mu V$. Due to the larger voltage criterion, $J_{c,Hall}$ is larger than J_c. Nevertheless, the overall functional dependencies of J_c and $J_{c,Hall}$ are the same for both orientations of antidot rows, except for the behaviour of the sign of the critical voltage (direction of vortex motion) and a small hysteretic jump in $J_{c,Hall}$ for one of the orientations of antidot arrows. This is discussed below.

$\gamma < 0°$: For these configurations (Fig. 2.20a), the Hall signal is negative over the whole investigated temperature range below T_c, the vortices moved in the direction of rows, indicated by the dashed red arrow in the sketch of Fig. 2.20a. The value of $J_{c,Hall}$ (corresponding to $V_{c,Hall} = -100\,\mu V$) increases monotonically with decreasing temperature. It agrees qualitatively with the behaviour of the critical current J_c in the superconducting state (black dashed line). The quantitative difference between J_c and $J_{c,Hall}$ is explained by differences in the voltage criteria ($V_c = 5\,\mu V/cm$ and $|V_{c,Hall}| = 100\,\mu V/cm$) and the different components of vortex motions (perpendicular or parallel to the Lorentz force) that are characterized.

$\gamma > 0°$: In this case (Fig. 2.20b), a different vortex behaviour is observed. The Hall voltage changes sign when cooling down from T_c. A negative voltage is observed close to T_c, when vortices do not follow the guidance of antidot rows. However, a few K below T_c, the Hall voltage changes abruptly to a positive value. The vortices move now in the direction imposed by antidot rows. This change of direction of vortex motion is hysteretic, i.e. it occurs at 83.7 and 84.4 K for decreasing and increasing temperatures, respectively. It is accompanied by a hysteretic change in the critical current $J_{c,Hall}$, seen in Fig. 2.20b, and a change of the microwave transmission coefficient S_{21} (not shown here) at exactly the same temperatures that indicate a change of the mobility of vortices [64]. The abrupt jump in the Hall voltage, critical current and microwave properties that is observed for the YBCO films with $\gamma > 0°$ suggests a change of the mechanism of vortex motion. It is discussed in the following.

Close to T_c, the negative Hall voltage is indicative of the presence of the AHE [94–103]. The vortex–antidot interaction is weak in this temperature range. Consequently, the guidance of vortex motion by the rows of antidots is negligible. The AHE dominates and vortices move in the direction defined by the AHE

as indicated in sample drawings of Fig. 2.20.[2] With decreasing temperature, the vortex–antidot interaction strength increases and, finally, the guidance of vortices via the rows of antidots starts to dominate the AHE. The vortices move within the rows of antidots [93].

When the orientation angle of antidot rows coincides with the direction of $<v>$ resulting in AHE, as is the case for the design of Fig. 2.20a, AHE and guided motion (GM) by antidot rows point in the same direction. Therefore, the Hall voltage stays negative over the whole temperature range, and changes in the critical current density and microwave properties are monotonous functions of T. In contrast, a change in the direction of motion is necessary when transition from AHE to guided motion occurs in the design of Fig. 2.20b. Close to T_c vortices shuttle between the rows of antidots, while below a certain temperature they move within the rows of antidots. This implies a modification of the mechanism of vortex motion. While vortices mainly travel in the superconductor in the first case, they "hop" from antidot to antidot in the latter case. This difference in the mechanism of vortex motion is visible in the resulting jumps in the critical current density and the microwave loss. The Hall critical current is modified by 10–12% at the transition. Vortex motion within the rows of antidots seems to be energetically more favourable than it is in the superconducting matrix [64].

Generally, guidance of vortices via antidot arrangements depends in a complicated way on the relation (amplitude and direction) of the different forces and potential acting on the vortices. The major forces to be considered are the "background" pinning force of the superconductor, the vortex–antidot interaction, driving forces (e.g. Lorentz force), Magnus force and thermal activation. Some of these interactions depend on temperature, and others on their orientation direction. This can lead to transition in the direction of vortex motion as function of temperature (Fig. 2.20), current density (see Fig. 2.21) or orientation of antidot arrangement (Fig. 2.22). As a consequence, guidance of vortices strongly depends upon temperature, driving force and geometrical arrangement of the antidots. If additionally anisotropic pinning potentials are introduced (e.g. via asymmetrically shaped antidots), preferentially directed vortex motion can be induced leading to ratchet effects or vortex diodes.

2.4 Vortex Matter in Superconducting Devices

In the previous sections, it has been shown that vortices easily penetrate into HTS thin film devices leading to vortex motion that will finally affect the performance of the device. For instance, it has been shown that vortex motion in active devices (e.g. SQUIDs and flux quantum logic) leads among others to increased low-frequency noise, reduced sensitivity or increased bit error rate [104, 105]. In

[2] It should be noted that only the direction but not the angle for this motion can be measured.

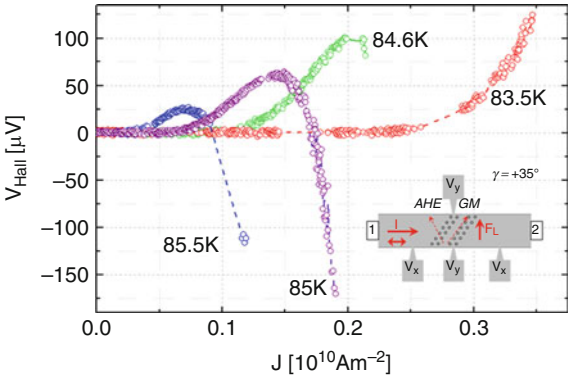

Fig. 2.21 Hall voltage of the sample shown in Fig. 2.20b as function of applied dc current density. A small magnetic field of 220 μT was applied; the arrangement of antidots is shown in the inset. At lower temperatures, a transition from guided motion (positive voltage) to AHE (negative voltage) is induced by the large driving forces, i.e. large current densities

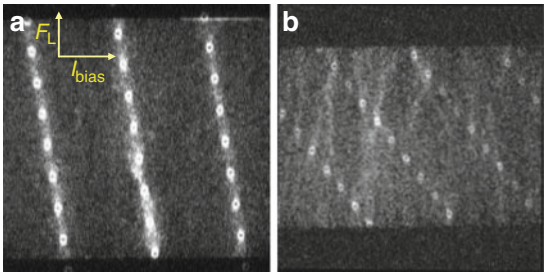

Fig. 2.22 Low temperature scanning microscopy images (area 200 × 200 μm^2) of YBCO films with rows of antidotes arranged at different angles $\gamma = -9°$ (**a**) and $\gamma = -38°$ (**b**) with respect to the Lorentz force [93]. Temperatures are 86 and 86.5 K, current density $J = 1.7\ J_c$ and $J = 1.2\ J_c$ in (**a**) and (**b**), respectively. Brighter regions correspond to higher amplitudes of the voltage response. In (**a**), the flux is guided along the rows of antidots, whereas in (**b**) flux starts to shuttle between adjacent rows (see *dashed ellipsoid*)

microwave devices (e.g. high-Q resonators, filters and antennas), vortices cause a reduction in the quality factor and power handling capability [57].

In this chapter, examples of active devices and passive microwave devices will be given that illustrate the role that vortices play in superconducting devices.

First, an efficient method for the reduction of *low-frequency noise* in *SQUIDs* will be described in which pinning of vortices by artificial defects is used. It will be demonstrated that (a) vortex motion is responsible for the low-frequency noise in SQUIDs and (b) an effective and field-independent noise reduction can be achieved by means of "strategically positioned" (thus, artificial) defects.

Second, *coplanar microwave resonators* are examined in small magnetic fields. It is shown that (a) the performance of these devices is strongly suppressed by vortices in the device and (b) a careful analysis of the local distribution of vortices in

the devices can be used for the understanding and optimization of the microwave properties of these devices.

Finally, concepts for novel *fluxonic devices* working at low and high frequencies are sketched. These concepts are based on vortex manipulation using various antidots arrangements. Especially the use of non-isotropic shapes or arrangements of antidots could lead to vortex ratchet effect, vortex-based rf-dc converter, microwave filter devices and many more interesting applications.

2.4.1 Low-Frequency Noise in SQUIDs

Superconducting quantum interference devices (SQUIDs) represent the most sensitive sensors of magnetic flux or small physical quantities that can be transformed into magnetic flux. They are of special interest in applications where extremely small magnetic fields have to be detected, e.g. non-destructive testing (NDE), geomagnetic applications and, especially, medical or biomagnetic applications (Fig. 2.23). For an overview on the working principle and the application of SQUIDs, the reader should refer to [104, 105]. Here, only a brief introduction into the concept of SQUIDs and the problem of vortex motion in SQUIDs is given.

The SQUID is a deceptively simple device, consisting of (1) a small superconducting loop with (2) one (rf-SQUID) or two (dc-SQUID) damped (resistively shunted) Josephson junctions. Magnetic flux threading the superconducting loop is always quantized in units of Φ_o. Thus, the total flux in the SQUID consists of the measured flux Φ plus the flux Φ_{ind} that is induced by current in the loop to

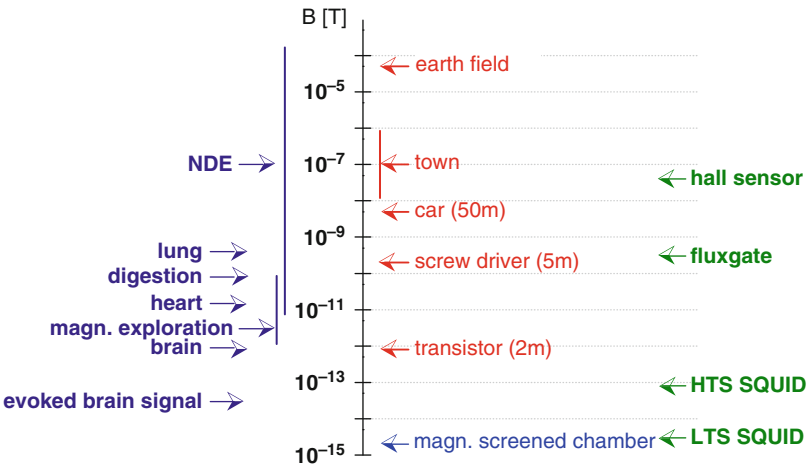

Fig. 2.23 Comparison of the magnetic-field sensitivity of conventional and superconducting field sensors (*right*), level of magnetic-field noise (*middle*) and field sensitivity required for various applications (*left*)

compensate according to: $\Phi_{tot} = n\Phi_o = \Phi + \Phi_{ind}$. The phase difference $\Delta\varphi$ across the Josephson junction is correlated with the superconducting tunnel current I_c according to the first Josephson equation [106]:

$$I_c = I_o \sin(\Delta\phi) = I_o \sin\left(\frac{\pi\Phi}{\Phi_o}\right) \tag{2.23}$$

with the tunnel current I_o at zero phase difference being a characteristic property of the contact and a phase that depends upon the magnetic flux in the contact according to $\Delta\varphi = \pi\Phi/\Phi_o$.

The SQUID makes use of the Josephson effect. By reading out the tunnel current (or related quantities), the magnetic flux is given in units of $\Phi_o = 2.068\times10^{-15}$ Wb. At a constant bias current, the voltage across the Josephson junction is periodically modified in a dc SQUID (Fig. 2.24) and the flux quanta in the SQUID loop can be counted. Moreover, in conjunction with suitable feedback electronics bucking the measured flux to maintain a stable operating point, the device can be used as a linear null detector. In this so called flux-lock-loop (FLL) mode, it becomes the most sensitive fluxmeter known, with a capability of resolving better than $10^{-6}\Phi_o$. The ranges of measured signal frequencies and intensity are wide and principally only limited by the electronics used. Typical room temperature electronics offer a frequency range extending from dc to kHz, and a dynamic range of 120 dB or more [105].

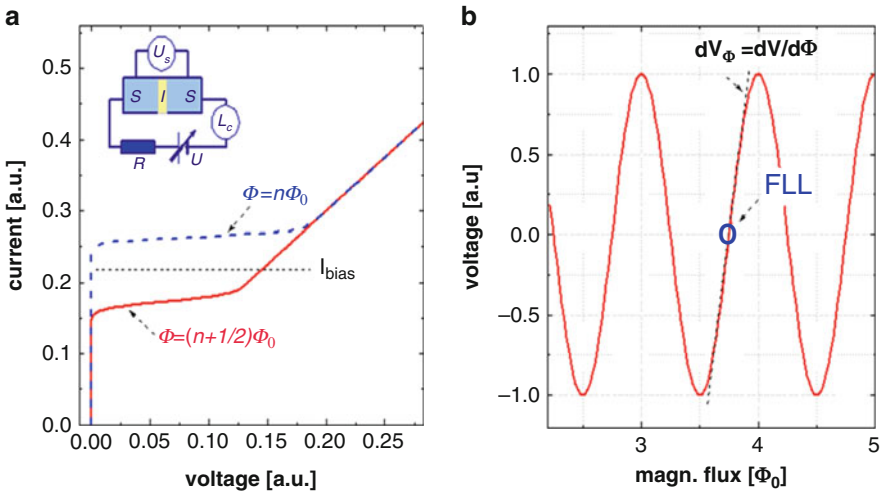

Fig. 2.24 Schematic drawing of the working principle of SQUIDs. The nonlinear IVC of a Josephson junction depends strongly on the magnetic flux (**a**). The superconducting tunnel current I_s changes periodically with the flux that threats the junction (**b**) (2.23). This periodical change is recorded in the SQUID for instance by applying an adequate bias current. The sensitivity of the SQUID can be enhanced using a feedback electronic (FLL) to fractions of the magnetic flux quantum $\Phi_o = 2.068 \times 10^{-15}$ Wb

In order to couple sufficient magnetic flux with a SQUID, either flux transformers are added or the superconducting loop (washer) is extended to provide sufficient flux focusing. Without going in detail (see e.g. [104, 105]), in both cases the inductance of the different components plays an important role and determines the final design of the device. In the first case, the large inductance of the transformer has to be matched to the SQUID inductance, i.e. large transformers with large inductance require SQUIDs with comparable inductance (i.e. SQUID of larger size). In the second case, the inductance of the extended washer has to be minimized to minimize the SQUID noise. The inductance of the SQUID is dominated by the diameter of the SQUID hole [107]. In both cases, the resulting SQUID possesses a large outer dimension (e.g. large focusing effect) and a small hole (small inductance). In conclusions, SQUIDs designed for technical applications generally posses rather extended structures (especially washers) that allow vortex to penetrate the superconductor. As a consequence, vortex motion within the superconductor plays a major role in these devices leading to a significant reduction in the SQUIDs sensitivity, especially for measurements that are performed at low frequencies.

Generally, the sensitivity of SQUIDs is limited by the frequency-dependent noise level of the device. Additional to the contribution of the electronics (usually white noise), in superconducting active devices two different sources are considered to be responsible for the noise. These are the contribution of the active part of the device, which usually consists of Josephson junctions, and the noise of the passive component, the superconducting thin film. The noise mechanisms in Josephson junctions are well understood [108–111] and a reduction in this noise contribution by simple electronic means has successfully been demonstrated [112–117]. The contributions of the superconducting thin film (mainly washer or flux transformer) to the noise of active devices are basically understood. They contribute to the low-frequency noise and are ascribed to motion of quantized flux (vortices) in the superconducting thin films. A nice illustration of this contribution is given by the so-called telegraph noise that occurs when a vortex hops between two pinning sites (Fig. 2.4b). In case of a statistical motion of many vortices, a scaling of the spectral noise density S_Φ with frequencies f and the applied magnetic field B is expected:

$$\sqrt{S_\Phi(f, B)} \propto \frac{B^n}{f^m} \tag{2.24}$$

with $n = m = 0.5$. This so-called $1/f$ noise-spectrum is ascribed to an incoherent superposition of many thermally activated microscopic fluctuators, which are given by moving or hopping vortices. The characteristic $1/f$ frequency dependence is evidence for a distribution of activation energies for the vortex hopping [118, 119]. Since most measurements of $1/f$ noise are sensitive only to small activation energies, usually only the low-energy part of this distribution is probed [120].

Typical examples of the spectral noise density and field dependences of the $1/f$ integral noise of rf-SQUIDs designed for applications are given in Fig. 2.25. The $1/f$ low-frequency noise is limited by the corner frequency (10–20 Hz at zero-field) above which the frequency-independent white noise sets in. The low-frequency

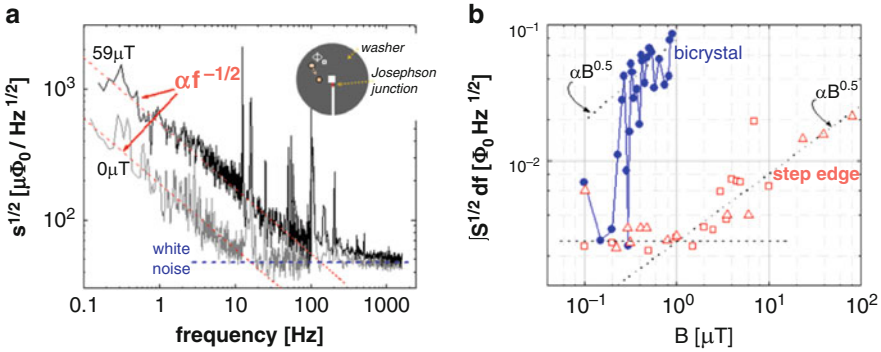

Fig. 2.25 (**a**) Spectral noise density for different magnetic fields measured in a HTS step-edge type rf-SQUID [52]. The lines idealize the different noise contributions, i.e. the field-dependent $1/f$ low-frequency noise and the field- and frequency-independent white noise. The schematic drawing sketches the geometry of the rf-SQUIDs and the problem of moving vortex in the washer. (**b**) Magnetic field dependencies of the integral noise of a step-edge and bicrystal Josephson junction according to [52]. The noise data are characterized by the normalized integration of the noise spectra in the low-frequency regime between 0.5 and 10 Hz. The *dotted lines* represent the theoretical field dependence of the low-frequency noise (2.24)

noise increases with increasing field for SQUIDs with extended washer, i.e. SQUIDs that are designed for application. This is demonstrated in Fig. 2.25b for two different types of SQUIDs, i.e. step edge and bicrystal type rf-SQUIDs [52]. For magnetic fields larger than the penetration field, the noise increases according to the theoretical expectation, i.e. $S_\Phi \propto B$ (2.24). The low-frequency noise represents a serious limitation for a number of applications of SQUIDs especially if the sensors are used in unshielded or barely shielded environment.

Various remedies to reduce the low-frequency noise have been suggested and tested that can be classified into two categories:

1. Either vortex penetration of the superconductor has to be avoided [121, 122] or
2. Vortices have to be pinned by sufficiently strong pinning sites in the superconductor [52, 89, 123]

In case of flux avoidance, extremely good screening or, alternatively, relatively small superconducting geometrical structures are required. Both solutions are technically difficult to realize and very costly. For instance, the patterning of the complete washer into a "grid" of striplines of linewidth $w < 6\,\mu\text{m}$ [124] would be necessary for application of these devices in earth field ($50\,\mu\text{T}$). This turns out to be technically quite complicated considering the requirements of the patterning. An alternative is given by vortex pinning at strong pinning sites. In the following, we will describe that (i) the low-frequency noise in SQUIDs can be modified via flux pinning due to artificial pinning sites (antidots) and (ii) only a few pinning sites very effectively suppress the low-frequency noise if they are strategically positioned in the SQUID.

2.4.1.1 Manipulation of the Low-Frequency Noise via Antidot Arrays

In order to demonstrate the effect of vortex–antidot interaction upon the low-frequency noise in HTS devices, a characteristic property of bicrystal rf-SQUIDs (BS) is exploited. At extremely small magnetic fields ($B_{p,GB} \approx 200\,nT$ for the BS used in the following experiment) clearly below the penetration field ($B_{p,SE} \approx$ 1–2 μT, see Fig. 2.25b), at which flux penetrates the washer in step-edge SQUIDs (SES) of identical geometry, the grain boundary in the washer of the BS serves as a channel for flux motion. This flux motion causes a drastic increase in 1/f noise (Fig. 2.25b). Once flux has penetrated the gain boundary, the further increase in the low frequency noise with field agrees with the expected field dependence $S_\Phi \propto B$ (2.24).

In order to examine the impact of the interaction between an antidot array and vortex lattices on the flux noise in a SQUID, a YBCO film with a square lattice ($d_{AA} = 5\,\mu m$) of antidots is mounted in flip-chip configuration on top of the grain boundary of the BS washer (see sketch in Fig. 2.26). For these measurements, the square antidot lattice is oriented with one axis along the grain boundary.

The resulting low-frequency noise-spectra of the arrangement (BS with antidot lattice) are given in Fig. 2.26. As expected, the lowest flux noise is recorded for zero magnetic field. At non-zero field, the low frequency noise strongly depends upon the exact values of the applied magnetic induction. In contrast to the standard field dependence $S_\Phi \propto B$ (2.24), it varies non-monotonically and over several orders of magnitude in noise level. For example, the noise at fields of 750 or 900 nT is more than 2 orders of magnitude larger than for the matching fields M_1 and M_2 (828 and 845 nT, respectively) at which the noise level of the zero-field spectrum is recorded.

A comparison of the field dependence of the low-frequency noise of the bare SQUID and the same SQUID with the antidot lattice is given in Fig. 2.27. In contrast to the reference measurements on the bare SQUID, which show the usually observed behaviour (i.e., constant noise level below $B_{p,GB}$ and linear increase $S_\Phi \propto B$ above $B_{p,GB}$), the data display clear minima and maxima. The minima are observed exactly at matching conditions. Matching or commensurability occurs when the vortex lattice matches the antidot lattice and the grain boundary, along which the "noisy" motion of the vortices takes place. Since the vortex lattice parameter $a_o \propto B^{1/2}$ varies with magnetic field, the resulting matching conditions can easily be recorded. They are listed in the table in Fig. 2.27. It should be noted that extremely small matching fields down to $247\,nT = B_1/324$ can be observed in this experiment. The noise level at matching fields is comparable to the noise level recorded at zero field. This indicated that vortex motion within the grain boundary of the washer is completely suppressed at matching condition. In contrast, at fields between the matching fields even larger noise levels (up to ten times larger) are observed for the SQUID with antidot lattice with respect to the bare SQUID. Thus, vortex motion is even enhanced in case of incommensurability between vortex lattice, antidot array and grain boundary. We can conclude as follows:

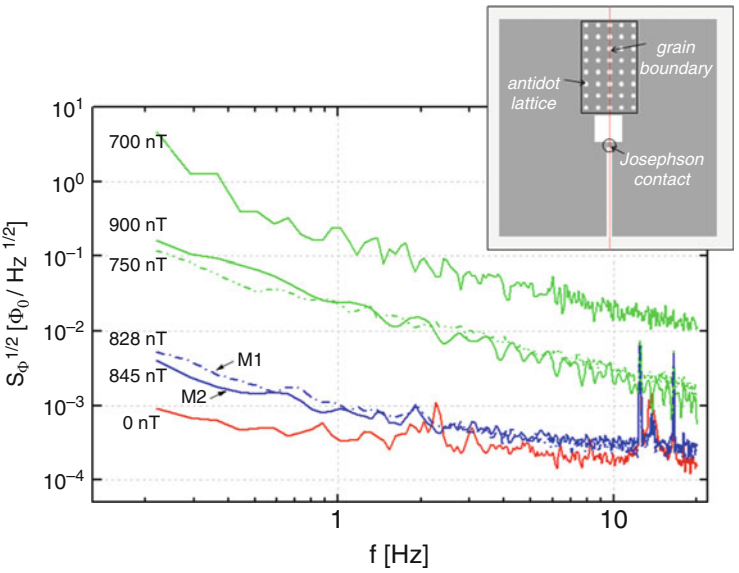

Fig. 2.26 Low-frequency noise spectra of a bicrystal rf-SQUID (BS) with a square antidots lattice on top of the grain boundary of the washer for different magnetic fields [89]. M_1 and M_2 label two matching conditions (see Table 2.1 in Fig. 2.27). The inset shows a sketch of the experimental arrangement. A YBCO film with square antidot lattice ($d_{AA} = 5\,\mu m$) is mounted in flip-chip configuration on top of the grain boundary of the BS. One of the main axes of the antidot lattice is oriented parallel to the grain boundary

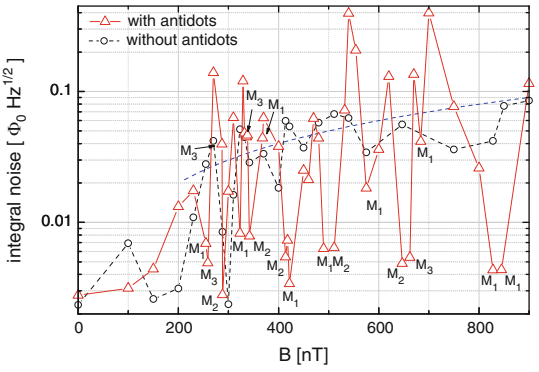

n	M_1	M_2	M_3	M_4
	a_0=d	a_0=	a_0=	a_0=
4				518 nT
5			662nT	331 nT
6			460nT	
7		845nT	338nT	
8		647nT	259nT	
9		511nT		
10	828nT	414nT		
11	684nT	342nT		
12	575nT	288nT		
13	490nT			
14	422nT			
15	368nT			
16	323nT			
17	287nT			
18	256nT			

Fig. 2.27 Magnetic field dependence of the normalized and integrated (0.5–10 Hz) low-frequency noise of a bicrystal rf-SQUID with and without an additional YBCO layer with an antidot lattice [89]. The noise data are measured several times and could be reproduced within the experimental error. The *blue dashed line* represents the theoretical field dependence $S_\Phi \propto B$ (2.24) of the SQUID without antidot lattice. The table represents the matching fields M_i with $I = 1$–4 in the field range between 255 and 900 nT. They are calculated for different vortex configurations (see schematic sketch) that match the square antidot array ($d_{AA} = 5\,\mu m$)

1. Noise manipulation via antidot lattices is demonstrated for HTS SQUIDs:
   (a) In case of commensurability between vortex and antidot lattice the flux noise is reduced to zero-field level
   (b) In case on non-commensurability, the noise level is even enhanced with respect to the noise of the SQUID without antidots lattice.
2. The noise measurements demonstrated commensurability effects between vortex and antidot lattices down to extremely small magnetic fields (i.e. fractions of the first matching field $\sim B_1/324$).
3. For noise reduction in SQUID applications working in variable magnetic fields, regular lattice of antidots are not suitable. Minima in the noise level at matching fields alternate with excessively high noise-levels for non-commensurability. Different solutions to this problem have been discussed, such as non-regular antidot lattices, extended holes or moats or the use of a few *strategically positioned* antidots. The latter is demonstrated in the next section.

2.4.1.2 Noise Reduction via Strategically Positioned Antidots

In the previous section, it was demonstrated that the low-frequency noise in SQUIDs can be manipulated via antidots. However, it can be seen in Figs. 2.26 and 2.27 and it is obvious from theoretical considerations that regular arrays of antidots lead to noise reduction only at discrete values of the magnetic field (at matching fields), whereas in case of non-commensurability between the vortex and antidot lattice even an increase in the low-frequency noise is observed. Therefore, it is better to use only a few "strategically positioned" antidots in the superconducting device, which trap only those vortices that attribute strongly to the low-frequency noise (i.e. vortices close to the SQUID hole) and leave the vortex lattice free to arrange itself within the device. Thus, the important issue is to allocate those strategic positions. A nice experimental demonstration for noise reduction via strategically positioned antidots is given in [52, 53, 89] for the case of rf-SQUIDs. It is sketched in the following.

Noise reduction by vortex trapping: Generally, the largest impact of vortex motion upon the SQUIDs flux noise is expected for vortex motion at a position close to the SQUID hole and Josephson junction. Vortex motion at this position (a) is more likely due to the large Lorentz force (caused by the read-out current) and (b) will lead to large flux changes at the Josephson contact [52]. Thus, obviously the first choice for strategically positioned antidots would be a position close to the Josephson junction and close to the SQUID hole. Figure 2.28 shows the corresponding arrangements of "strategically positioned" antidots and the resulting modification of the noise properties determined via field-cooled experiments.

The resulting noise reduction can be seen in *field-cooled* experiments in Fig. 2.28b. In these experiments, the SQUID is cooled from the normal to the superconducting state in an applied field B oriented normal to the film surface.

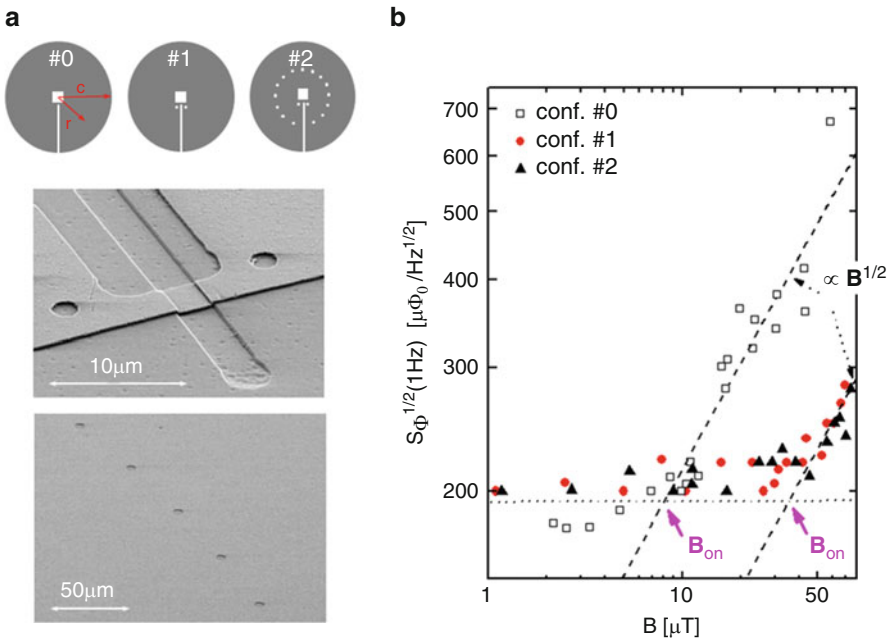

Fig. 2.28 (**a**) Sketch of a YBCO rf-SQUID with different antidot configurations [without antidots (#0), with two antidots in the vicinity of the junction (#1) and, finally, two antidots at the junction and an additional ring of antidots at radial position $r = c/2$ (#3)]; SEM images of the two antidots in the vicinity of the junction (antidots radius $r_o = 750\,\text{nm}$) and the ring of antidots ($d_{AA} = 50\,\mu\text{m}$, $r_o \sim 1.25\,\mu\text{m}$). (**b**) Spectral noise density at 1 Hz ($1/f$ noise) as a function of the magnetic field for field-cooled measurements and the different configurations of strategically positioned antidots. The onset of the increase in the low-frequency noise is characterized by the onset fields B_{on} for the different configurations. The proportionality $S_\Phi \propto B$ of the low-frequency noise for $B > B_{on}$ (*dashed lines*) agrees with the theoretical expectation in (2.24). The onset field for the configurations with antidots (#1 and #2) is comparable to the earth field of $\sim 50\,\mu\text{T}$

A comparison of the spectral noise density in the low-frequency regime ($1/f$ noise) for a SQUID with the different successively patterned antidot arrangements demonstrates[3]:

1. At low fields $B < B_{on}$, the spectral noise density is field independent and the same for all configurations.
2. At higher fields $B > B_{on}$, the spectral noise densities increase linearly with increasing field according to the theoretical expectation $S_\Phi \propto B$.
3. However, the transition from field-independent to field-dependent spectral noise density is significantly increased from $B_{on} \approx 8\,\mu\text{T}$ for configuration #0 (without antidots) to $B_{on} \approx 40\,\mu\text{T}$ for the configurations with antidots (#1 and #2).

[3] Note that always the same SQUID has been used in this experiment.

The significant increase in the onset field B_{on} by the arrangement of only two strategically positioned antidots is sufficient for most applications of SQUIDs in unshielded environment (earth field $B_{earth} \approx 50\,\mu T$).

Usually SQUIDs are used in varying field. As a consequence, flux will penetrate the SQUIDs' washer when the magnetic field is changed; this automatically leads to enhanced flux noise due to vortex motion. A detailed discussion of this effect including the possibility of determining the position of individual vortices in the washer is given in [52, 53, 89]. One solution for this problem is the operation of the SQUID in the so-called flux-lock-loop. Using a feedback electronic, the flux is kept constant at the SQUID. Nevertheless, large or sudden flux changes cannot always be avoided. As a result, the SQUID will be "noisy" for a long time or has to be warmed up to the normal state to remove unwanted flux in the washer. An alternative is given by introducing a ring of antidots at a constant radial position (see configuration #2 in Fig. 2.28). It allows the vortices to (1) easily enter the washer without and (2) modify the flux in the SQUID hole once the vortex is in the washer. As a consequence, a change in the applied magnetic field would only result in brief increase of the noise density followed by the fast reduction of the flux noise to the operation level. This effect has been demonstrated for configuration 2 (Fig. 2.28) for magnetic fields up to 24 μT [52].

In conclusion of this section, the noise of SQUIDs proved to be extremely sensitive to vortex motion and commensurability effects of the vortex and antidot lattice. Even the position of vortices and their motion in the SQUIDs washer can be determined experimentally. As a consequence, extremely simple arrangements of only a few but well-positioned antidots lead to a considerable reduction of flux noise in HTS SQUIDs. For instance, a pair of antidots arranged in the vicinity of the Josephson junction of rf-SQUIDs strongly reduces the $1/f$ noise in ambient magnetic fields, and well-directed penetration of vortices in the washer can be achieved via rows of antidot. Thus, vortex manipulation in HTS SQUIDs is a powerful tool to improve the performance of these devices.

2.4.2 Vortex Matter in Microwave Devices

The behaviour of a conductor in a microwave field can generally be characterized by the complex surface impedance $Z_s = R_s + iX_s$ with surface resistance R_s and surface reactance X_s. Z_s describes the electrodynamics at the interface between vacuum and (super)conductor. The surface resistance represents the dissipated energy, whereas the surface reactance characterizes the energy stored in the conductor. The surface resistance is given by:

$$R_s = X_s = \sqrt{\frac{2\pi^2 \mu_0 f}{\sigma_n}} \text{ and } R_s \approx 2\pi^2 \mu_o^2 f^2 \sigma_n \lambda^3 \tag{2.25}$$

for the normal conductor and superconductor (two-fluid model), respectively. Here, f represents the frequency and σ_n is the conductivity due to normal charge carriers.

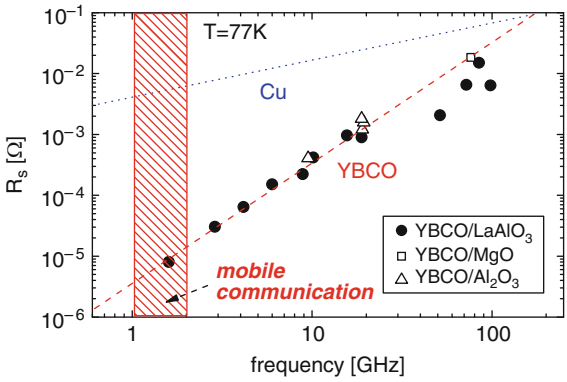

Fig. 2.29 Comparison of the frequency dependence of the microwave surface resistance R_s at $T = 77$ K for YBCO films on different substrates and Cu. The frequency regime used for mobile communication is marked

The surface resistance of a type-II superconductor and a normal conductor shows a significant difference in frequency dependence and magnitude. At frequencies up to a few GHz, technical superconductors (e.g. Nb, NbN and HTS) possess orders of magnitude smaller R_s values that automatically result in smaller microwave losses.

From this point of view, the superconductor offers a significant benefit in microwave applications. As demonstrated in Fig. 2.29, the smaller losses can be used to improve the quality factors $Q = f_o/\Delta f$ of resonators or filters (f_o represents the centre frequency and Δf is the full width of the resonance at -3 dB), or lead to miniaturization of existing devices [125, 126]. As a consequence, usually large power densities are encountered in HTS microwave devices. However, in contrast to their normal-conducting competitors, the power handling capability of superconducting microwave devices is limited by the nonlinearity of the surface resistance. At high microwave power, R_s increases significantly (Fig. 2.30). This not only leads to an increase in dissipated energy that finally causes a heating of the superconductor, but also causes a degradation of Q values and the development of unwanted intermodulation signals.

Although various physical origins are discussed (e.g. weak links, thermal or magnetic effects), the physical mechanism, which is responsible for the nonlinear surface resistance and that represents a serious restriction for a number of microwave applications, is not fully understood. Nevertheless, it has been demonstrated that vortex matter has a significant impact on the properties of HTS microwave devices, including the quality factor, the nonlinearity and the power handling capability [57]. In this section, we will give a few examples of experimental evidence for the vortex-induced modifications of microwave properties of HTS films and HTS devices. Then we will sketch possible ways to overcome these problems. Finally, we will demonstrate that one might use the impact of vortices on microwave properties to design novel microwave fluxonic devices.

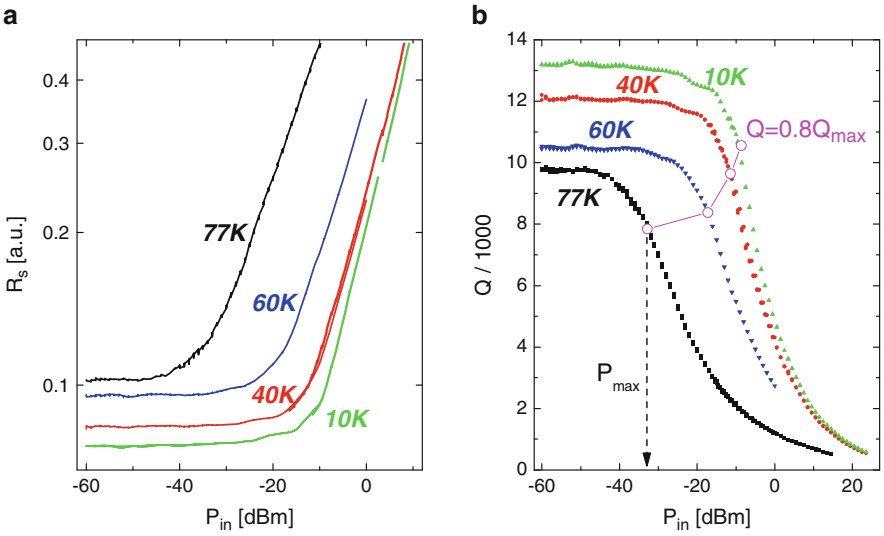

Fig. 2.30 The nonlinearity of the microwave surface resistance of HTS films leads to a degradation of the performance of superconducting devices at large microwave power. This is visible for instance in a significant increase of the surface resistance (**a**) and the degradation of the quality factor (**b**) measured in this example for a 1.6 GHz coplanar YBCO resonator

2.4.2.1 Impact of Vortices on the Microwave Properties

The basic components of microwave devices made from HTS thin films are impedance-matched stiplines. Due to the thickness and the dielectric properties of the substrate, an impedance of 50 Ω results in a typical width of the structures of $w = 300$–$600\,\mu$m. On the one hand, the microwave current is strongly peaked at the edge of the conductor. For example, the experimentally determined current densities in the central conductor of a coplanar microwave devices can be approximated by [127]

$$J_{\mathrm{rf}}(x) = \frac{I}{wK\left(\frac{w}{a}\right)} \begin{cases} \left[\left(1-\left(\frac{2x}{w}\right)^2\right)\left(1-\left(\frac{2x}{a}\right)^2\right)\right]^{-1/2} & |x| \le \frac{w}{2}-\lambda \\ \left[\left(1-\left(\frac{w}{a}\right)^2\right)\frac{\lambda}{w}\right]^{-1/2} & \frac{w}{2}-\lambda \le |x| \le \frac{w}{2} \\ -\left[\left(\left(\frac{a}{w}\right)^2-1\right)\frac{\lambda}{w}\right]^{-1/2} & \frac{a}{2} \le |x| \le \frac{a}{2}-\lambda \\ -\left[\left(\left(\frac{2x}{w}\right)^2-1\right)\left(\left(\frac{2x}{a}\right)^2-1\right)\right]^{-1/2} & |x| \ge \frac{a}{2}+\lambda \end{cases} \quad \text{for} \tag{2.26}$$

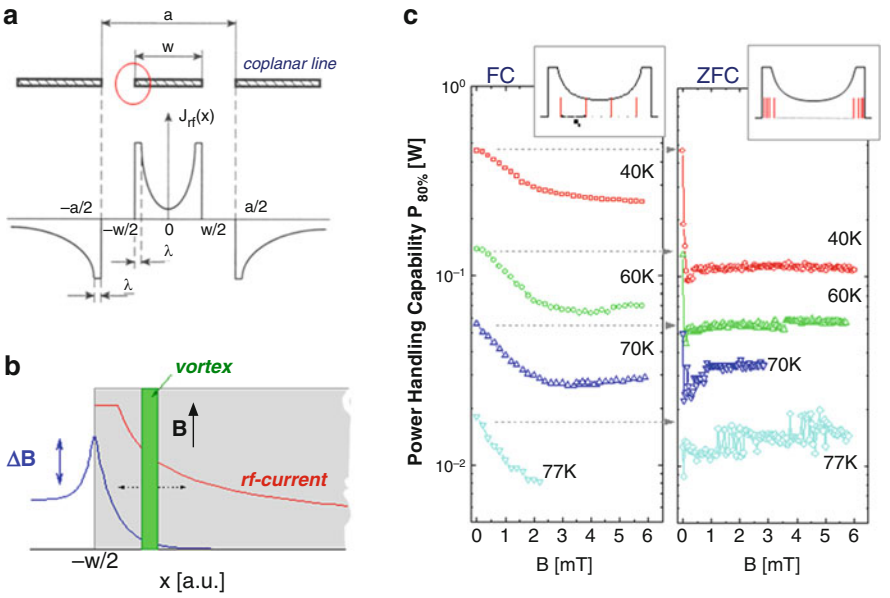

Fig. 2.31 Schematic drawing of (**a**) the microwave current distribution J_{rf} in a coplanar superconducting lines according to (31) and (**b**) the microwave current and magnetic field distribution at the edge of a superconducting stripline. (**c**) Field dependence of the power handling capability of a coplanar YBCO resonator for field-cooled and zero-field cooled experiments at different temperatures [57]. The sketches in (**c**) indicate the different vortex distribution in field cooled and zero-field cooled experiments and the microwave current distribution in the central conductor of the coplanar microwave resonator

with w representing the width of the stripline, a the distance between the ground planes and K the complete elliptical integral of the first kind. A sketch of the cross-section of the structure and the resulting microwave current distribution is given in Fig. 2.31a. On the other hand, vortices will penetrate at the edge of the superconducting stripline upon modification of the applied magnetic field. Due to the large aspect ratio, small changes of the external field will result in large changes of the magnetic field at the edge of the stripline. Depending on the position of the vortex, the microwave current will be affected differently. This situation is sketched in Fig. 2.31b.

Experimentally, it has been demonstrated by comparing *field-cooled* (fc) and *zero-field cooled* (zfc) measurements of the power handling capability of YBCO thin film microwave resonators that were exposed to small magnetic fields (Fig. 2.31c) [57]. In these experiments, the power handling is characterized by the degradation of the loaded quality factor $Q_L = f_o/\Delta f$, i.e. P_{max} is defined by the condition $Q_L(P_{max}) = 0.8\ Q_L(P_o)$ (see also Fig. 2.30b). In fc experiments, the resonator is cooled to the superconducting state in the applied magnetic field (i.e. the vortex distribution is expected to be homogeneous), whereas in zfc experiments the resonator is cooled to the superconducting state in zero-field and the magnetic field is applied

in the superconducting state. In the latter case, vortices have to penetrate from the edge of the superconductor, leading to an inhomogeneous distribution of vortices. Thus, the expected vortex distribution is different for fc and zfc experiments, and it is sketched in the insets of Fig. 2.31c.

The resulting power handling capability P_{max} depends strongly upon the way the magnetic field is established. While fc measurements show a gradual decrease of P_{max}, in zfc experiments a strong decrease of the power handling capability within a few μT is followed by an almost constant P_{max} (Fig. 2.31c). The different behaviours are consequences of the vortex distribution in the resonator. For fc experiments, the moderate increase in the homogeneous vortex density with increasing field seems to lead to the moderate and gradual decrease of P_{max}. In contrast to the fc experiments, an inhomogeneous vortex distribution is expected for the zfc experiment. Due to the flux penetration at the edge of the superconductor, in the zfc case the position of the largest vortex density coincides with the maximum of the rf current at the edge of the central conductor. This explains the strong reduction of P_{max} that is observed already at extremely small fields of a few μT. A further increase of the field in the zfc case does not affect the power-handling capability seriously. This is consistent with other observations of flux penetration at small fields, where an increase in the magnetic field first leads only to a shift of the flux front into the superconductor. Since the interior of the superconductor does not carry large rf currents, this shift does not affect the power handling capability seriously. Furthermore, the fc and zfc values of P_{max} seem to merge at large fields. This is expected for the field for which the zfc flux front approaches the centre of the sample. For these fields, similar vortex densities are expected at the edge of the superconductor for the fc and zfc case.

The complete picture of the impact of vortices on the properties of microwave resonators that also confirm the interpretation of the fc and zfc data given above is illustrated by field-cooled sweep (fcs) experiments. In fcs experiments, the sample is first cooled to the superconducting state in an applied field B_{fc} (where the field-cooled state is established) and, subsequently, the field is modified by ΔB. Figure 2.32 shows a typical example of fcs measurements together with fc and zfc data recorded for a 1.4 GHz YBCO coplanar resonator at 60 K. The zfc and fc data represent lower and upper values for the power handling capability, respectively, whereas fcs measurements start with the fc value and show a strong and complex variation of P_{max} that is shown in detail in the inset of Fig. 2.32. The behaviour of P_{max} in fcs experiments can be interpreted in terms of vortex penetration and annihilation caused by magnetic fields of the order of μT (for a detailed discussion, refer to [57]). It demonstrates that not only flux and vortices have a large impact upon the performance of a microwave device, but also the field direction and, especially, the correlation between the spatial distributions of vortices and microwave current density are of importance. The largest impact of vortices upon the microwave properties is observed for vortices at the edge of the microwave device that represents the part of the device that normally carries the highest microwave current density. As a consequence, vortices have to be manipulated (e.g. guided into the centre of the

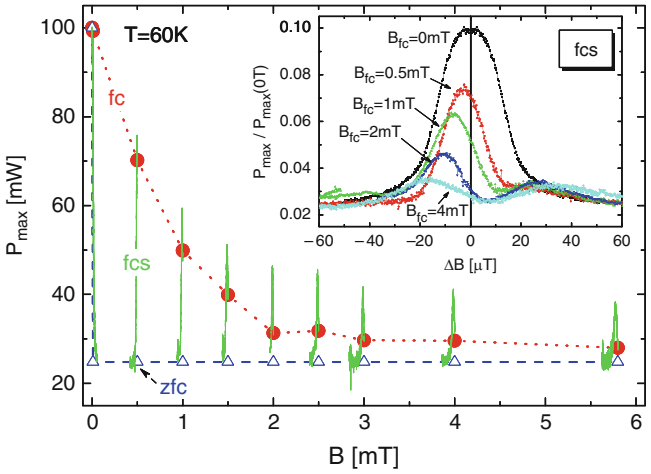

Fig. 2.32 Comparison of the magnetic field dependence of the power handling capability of a coplanar 1.4 GHz YBCO resonator for fc (*solid red circles*), zfc (*open blue triangles*) and fcs (*green lines*) experiments. The inset shows the power handling capability in fcs measurements for different starting fields B_{fc} on a normalized scale $\Delta B = B - B_{fc}$

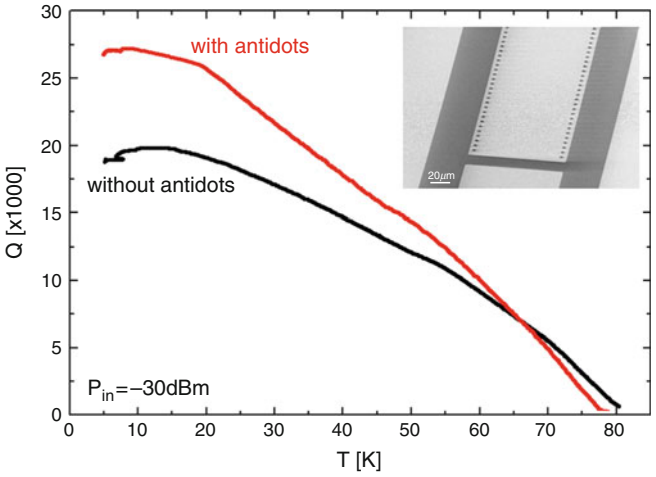

Fig. 2.33 Loaded quality factor of a 1.4 GHz YBCO resonator measured in small varying magnetic fields of the order of a few μT with and without antidots. The inset shows the arrangement of antidots that are positioned at the edge of the central line of the coplanar resonator

microwave device) to conserve the performance of microwave devices operating in magnetically unshielded environment. This situation is very similar to the situation encountered in SQUIDs where flux is guided into the washer by a row of antidots. First attempts to improve the performance of microwave resonators that are exposed to magnetically unshielded environment via antidots are demonstrated in Fig. 2.33.

2.4.2.2 Concepts for HTS Fluxonic Devices

In the previous sections, strategies to improve existing superconducting devices by manipulating (i.e. trapping and guiding) vortices were introduced. However, the field of vortex manipulation by micro- or nanostructures in HTS films is much more colourful. Different feasible concepts are sketched in Fig. 2.34. For instance, vortices might be generated, guided and trapped by slits, small and large antidots, respectively. By adequate magnetic field variations or using the current curls created by a slit at opposing edges of a stripline, even vortices and antivortices can be created and manipulated. The operation of some of these components has been demonstrated for low-T_c films (e.g. Nb, Pb or Al films) or their impact upon magnetic flux has been visualized by magneto-optic experiments [128, 129]. An interesting option is given using asymmetric antidots that could lead to the directed vortex motion, the so-called ratchet effect. This will be briefly sketched in this section.

Generally, *ratchets* are formed from spatially asymmetric confining potentials. They can rectify oscillatory driving forces and generate directed motion. Ratchet scenarios were already considered by Feynman in his lecture notes in 1963 [130] and are related to earlier problems of thermodynamic studied by Smoluchowski in 1912 [131]. Ratchets represent a major component of particle transport in nanoscale systems, both in solid-state systems and in biology. Ratchets in biological systems (e.g. biomolecular motors) can be found in nature, including the kinesin and dynein proteins that provide transport functions within the cell [132]. Ratchets can be produced by biomolecular engineering, e.g. molecular walker constructed from strands of DNA [133] and controlled motion of kinesin-driven microtubules along lithographically patterned tracks have been demonstrated recently [134]. Advances in nanofabrication made it feasible to develop and investigate ratchets formed from

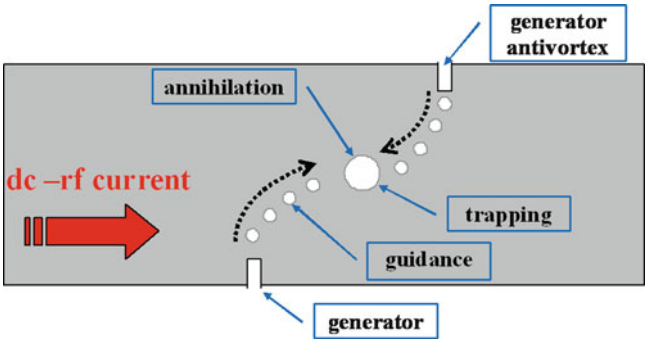

Fig. 2.34 Sketch of different nano- and microstructure components for vortex manipulation in HTS films that might lead to novel fluxonic applications. Vortices and antivortices (vortices with inverted field component) can be generated by curls in the dc or microwave current caused by slits at opposite edges of a stripline. Guidance and trapping are achieved by antidots of different size. Annihilation of vortices would be possible in case of guidance of vortex and antivortex towards the same trapping site

solid-state systems involving electronic devices or microfluidics. Such devices can be used (1) as analogue systems for modelling biomolecular motors, (2) to understand novel particle transport at the nanoscale or (3) to develop new devices for application. One advantage of solid-state nanofabrication is the possibility to tailor the ratchet potential and to control driving parameters, temperature or other process parameters. Implementations of ratchets in electronic devices have been demonstrated recently, e.g. the use of asymmetric structures of electrostatic gates above a 2D electron gas [135] and arrays of Josephson junctions with asymmetric critical currents [136].

Vortices in superconductors form an ideal system for exploring ratchet phenomena. The control of vortex dynamics via micro or nanostructures allows for the tailoring of vortex confining potentials. One approach for controlling and rectifying vortex motion in superconductors involves the use of arrays of antidots. Vortex ratchet effects obtained by various arrangements of antidots have recently been demonstrated for low-T_c films [48–51] and high-T_c films [33]. The asymmetric pinning potential is achieved by asymmetrically shaped antidots, combinations of antidots of different sizes, asymmetric arrangement of symmetric antidots or even mixing of dc and ac currents

Figure 2.35 shows an example of a HTS ratchet that also illustrates the potential use of ratchets in microwave applications. The design of the device (Fig. 2.35a) is similar to the design used for the demonstration of guided vortex motion (Fig. 2.19), except for the fact that asymmetric (here, triangular shaped) antidots are used. The

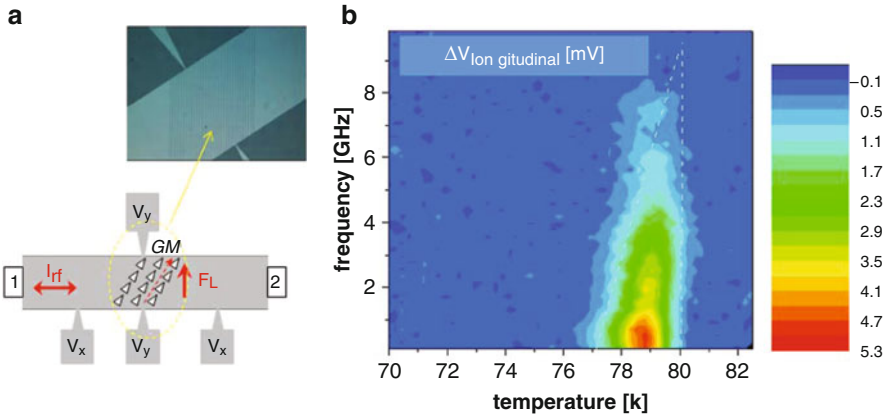

Fig. 2.35 Demonstration of the ratchet effect in HTS microwave devices. Schematic drawing and microscope image of a YBCO ratchet based on rows of triangular-shaped antidots (**a**) and contour plot of the change of the dc voltage signal $\Delta V_{\text{longitudinal}} = V_{\text{longitudinal}}(-10\,\text{dBm}) - V_{\text{longitudinal}}(-50\,\text{dBm})$ as function of temperature and applied microwave frequency (**b**). The microwave current is applied via ports 1 and 2, the vortices are rectified by rows of triangular antidots and the dc longitudinal and dc Hall voltages are recorded at contacts V_x and V_y. The microscope image shows the stripline in the vicinity of the Hall contacts. The change in the rectified longitudinal voltage signal due to the microwave power demonstrates the rectified vortex motion for temperatures close to T_c (high vortex mobility) and up to frequencies of about 10 GHz

tilting of the direction of antidot rows with respect to the Lorentz force allows for simultaneous measurements of a longitudinal and Hall signal in case of guided vortex motion. In case of a rectification of the vortex motion (ratchet effect), a microwave driving current would be transformed in a directional motion of vortices and, thus, a dc voltage at the Hall and longitudinal voltage pads. Figure 2.35b shows a contour plot of the dc voltage (only the longitudinal voltage is shown) obtained in a typical experiment. In order to improve the resolution of the measurement, a reference signal taken at low microwave power (−50 dBm) is subtracted from the signal recorded at large microwave power (−10 dBm).

The experiment demonstrates that HTS vortex ratchets operate, although in a restricted temperature regime close to T_c and a frequency regime up to about 10 GHz. An obvious restriction of the operation regime is imposed by the limited microwave power used in the experiment. Close to T_c, the pinning force in small and vortices move easily. At lower temperatures, pinning force and viscosity increase and, as a consequence, larger microwave power is needed to move vortices between the antidots. This restricts the temperature regime for operation to temperatures close to T_c. Nevertheless, the temperature regime is still quite large compared to operation regimes of low-T_c films, where ratchet effects are typically present in the regime of $0.995 < T/T_c < 1$. Whether the frequency limit (∼10 GHz) is a fundamental limit for motion of Abrikosov vortices in HTS devices is not clarified till now. Experiments executed at larger microwave power or the use of smaller antidot distances might prove this in the future.

The principle of vortex ratchet is one of the most interesting components for basic analysis and maybe in the future also for application of vortex manipulation in HTS films and devices. Its operation has been demonstrated. HTS vortex ratchets might be used as a converter (microwave-to-dc), filters or as a component in more complex microwave devices that could offer interesting and novel properties.

2.5 Conclusions

Vortex matter in HTS films and devices not only is an interesting topic for basic research but also plays a substantial role for application of superconductivity in general. In most electronic applications, magnetic flux will penetrate the superconductor. Magnetic flux and flux motion affect the performance of superconducting devices. For instance, the reduction of the sensitivity in SQUIDs or the power-handling capability in microwave devices, or the increase of the error rate in logic devices is a consequence of the presence of flux and flux motion in these devices. Guidance and trapping of vortices can reduce or even prevent this effect.

Moreover, vortex manipulation not only is a useful tool to avoid degradation of HTS film and device properties, but can also be used to analyse and understand novel and interesting physical properties and to develop new concepts for application of HTS. Various concepts for vortex manipulation are sketched. The advantage of the use of micro- and nanopatterns (especially antidots) to guiding and trapping

of vortices is discussed, and experimental evidence of vortex guidance and vortex trapping by various arrangements of antidots is given.

Thus, the vortex state of matter appears to be very important in applications of superconductivity that requires further investigation. A better understanding will clearly lead to an improvement in the performance of HTS components, such as reduced noise, better power handling capability or improved reliability. Furthermore, it promises deeper insight into the basic physics of vortices and vortex matter, especially at high frequencies. The use of different experimental techniques in combination with micro- or even nanopatterning of high-T_c superconducting film might pave the way towards strategic manipulation of vortices. Systematic analysis of manipulation methods could in turn pave the route towards interesting and innovative fluxonic effects and device concepts.

Acknowledgements The author likes to acknowledge the experimental work of A.M. Castellanos, P. Selders, M. Pannetier, R. Wijngaarden, A. Pruymboom, P. Dymachevski and P. Lahl. Furthermore, A. Offenhäuser, A.I. Braginski, V.R. Misko, V. Yurchenkov, E. Hollmann and R. Kutzner are acknowledged for their support, cooperation and discussion. This work was supported by the ESF program "Nanoscience and Engineering in Superconductivity – NES".

References

1. J.G. Bednorz, K.A. Müller, Z. Phys. B **64**, 189 (1986)
2. H. Kamerlingh Onnes, Leiden Comm. **120b**, **122b**, **124c** (1911)
3. A.G. Lebed (ed.), The physics of organic superconductors and conductors. Springer Ser. Mater. Sci. 110 (2008), ISBN: 978-3-540-76667-4
4. D.E. Farrell, C.M. Williams, S.A. Wolf, N.P. Bansal, V.G. Kogan, Phys. Rev. Lett. **61**, 2805 (1988)
5. D.E. Farrell, S. Bonham, J. Foster, Y.C. Chang, P.Z. Jiang, K.G. Vandervoort, D.L. Lam, V.G. Kogan, Phys. Rev. Lett. **63**, 782 (1989)
6. D.E. Farrell, R.G. Beck, M.F. Booth, C.J. Allen, E.D. Bukowski, D.M. Ginsberg, Phys. Rev. B **42**, 6758 (1990)
7. K. Okuda, S. Kawamata, S. Noguchi, N. Itoh, K. Kadowaki, J. Phys. Soc. Japan **60**, 3226 (1991)
8. J.G. Ossandon, J.R. Thompson, D.K. Christen, B.C. Sales, H.R. Kerchner, J.O. Thomson, Y.R. Sun, K.W. Lay, J.E. Tkaczyk, Phys. Rev. B **45**, 12534 (1992)
9. E. Zeldov, A.I. Larkin, V.B. Geshkenbein, M. Konczykowski, D. Majer, B. Khaykovich, V.M. Vinokur, H. Shtrikman, Phys. Rev. Lett. **73** 1428 (1994)
10. N. Kokubo, Phys. Rev. Lett. **88**, 247004 (2002)
11. K. Yu, T.W. Heitmann, C. Song, M.P. DeFeo, B.L.T. Plourde, M.B.S. Hesselberth P.H. Kes, Phys. Rev. B **76**, 220507 (2007)
12. V.V. Yurchenko, A.J. Qviller, Y. Galperin, P. Mozhaev, J.B. Hansen T.H. Johansen, Effect of self-organized periodic pinning arrays on magnetic flux dynamics in high-T_c superconductors (to be published)
13. R. Besseling, Thesis, University of Leiden (2001)
14. M. Baert, V.V. Metlusko, R. Jonckheere, V.V. Moshchalkov, Y. Bruynseraede, Phys. Rev. Lett. **74**, 3269 (1995)
15. A.M. Castellanos, R. Wördenweber, G. Ockenfuss, A. v.d. Hart, K. Keck, Appl. Phys. Lett. **71**, 962 (1997)
16. R. Wördenweber, P.H. Kes, C.C. Tsuei, Phys. Rev. B **33**, 3172 (1986)

17. R. Wördenweber, P.H. Kes, Phys. Rev. **B34**, 494 (1986)
18. D. Dew-Hughes, Philos. Mag. **30**, 293 (1974)
19. A.I. Larkin, N. Yu, J. Ovchinnikov, Low Temp. Phys. **34**, 409 (1979)
20. H. Kronmüller, M. Fähnle, M. Domann, G. Grimm, R. Grimm, B. Gröger, J. Magn. Magn. Mater. **13**, 53 (1979)
21. G. Blatter, M.V. Feigel'man, V.B. Geshkenbein, A.I. Larkin, V.M. Vinokur, Rev. Mod. Phys. **66**, 1125 (1994)
22. P.H. Kes, J. van den Berg, in *Studies of High Temperature Superconductors*, vol. 5, ed. by A. Narlikar (NOVA Science Publishers, New York, 1990), p.83
23. E.H. Brandt, U. Essmann, Phys. Status Solidi B **144**, 13 (1987)
24. E.J. Kramer, J. Nucl. Mater. **72**, 5 (1978)
25. A. Pruymboom, P.H. Kes, E. van der Drift, S. Radelaar, Appl. Phys. Lett. **52**, 662 (1988); Phys. Rev. Lett. **60**, 1430 (1988)
26. D.O. Welch, J. Adv. Sci. **4**, 81 (1992)
27. R. Wördenweber, Phys. Rev. B **46**, 3076 (1992)
28. R. Wördenweber, Rep. Prog. Phys. **62**, 187 (1999)
29. R. Gross, J. Bosch, H.-G. Wener, J. Fischer, R.P. Hübener, Cryogenics **29**, 716 (1989)
30. M.P. González, E. Hollmann R. Wördenweber, J. Appl. Phys. **102**, 063904 (2007)
31. F. Laviano, G. Ghigo, E. Mezzetti, E. Hollmann, R. Wördenweber, Engineering confined vortex flow in YBCO films patterned by heavy-ion lithography (to be published)
32. R. Wördenweber, A.M. Castellanos, P. Selders, Physica C **332**, 27 (2000)
33. R. Wördenweber, P. Dymashevski, V.R. Misko, Phys. Rev. B **69**, 184504 (2004)
34. T. Haage, J. Zegenhagen, J.Q. Li, H.-U. Habermeier, M. Cardona, C. Jooss, R. Warthmann, A. Forkl H. Kronmüller, Phys. Rev. B **56**, 8404 (1997)
35. J.I. Martín, M. Vélez, J. Nogués I.K. Schuller, Phys. Rev. Lett. **79**, 1929 (1997)
36. M. Andersson, J.C. Cuevas M. Fogelström, Physica C **367**, 117 (2002)
37. M. Lange, M.J. Van Bael, Y. Bruynseraede V.V. Moshchalkov, Phys. Rev. Lett. **90**, 197006 (2003)
38. E. Rosseel, M. van Bael, M. Baert, R. Jonckheere, V.V. Moshchalkov, Y. Bruynserade, Phys. Rev. B **53**, R2983 (1996)
39. V.V. Metlushko, M. Baert, R. Jonckheere, V.V. Moshchalkov, Y. Bruynserade, Solid State Commun. **91**, 331 (1994)
40. V.V. Moshchalkov, M. Baert, E. Rosseel, V.V. Metlushko, M.J. van Bael, Y. Bruynserade, Physica C **282**, 379 (1997)
41. V.V. Moshchalkov, M. Baert, V.V. Metlushko, E. Rosseel, M.J. van Bael, K. Temst, Y. Bruynserade, R. Jonckheere, Phys. Rev. B **57**, 3615 (1998)
42. V.V. Moshchalkov, M. Baert, V.V. Metlushko, E. Rosseel, M.J. van Bael, K. Temst, R. Jonckheere, Y. Bruynserade, Phys. Rev. B **54**, 7385 (1996)
43. L. van Look, E. Rosseel, M.J. van Bael, K. Temst, V.V. Moshchalkov, Y. Bruynseraede, Phys. Rev. B **60**, R6998 (1999)
44. A. Bezryadin, B. Pannetier, J. Low Temp. Phys. **98**, 251 (1995)
45. W. Lang, J. Pedarnig, *Ion Irradiation of High-Temperature Superconductors and Its Application for Nanopatterning* (this book)
46. J.F. Wambaugh, C. Reichhardt, C.J. Olson, F. Marchesoni, F. Nori, Phys. Rev. Lett. **83**, 5106 (1999)
47. J.E. Villegas, S. Savel'ev, F. Nori, E.M. Gonzalez, J.V. Anguita, R. García, J.L. Vicent, Science **302**, 1188 (2003)
48. B.Y. Zhu, F. Marchesoni, V.V. Moshchalkov F. Nori, Phys. Rev. B **68**, 014514 (2003)
49. J. Van de Vondel, C.C. de Souza Silva, B.Y. Zhu, M. Morelle V.V. Moshchalkov, Phys. Rev. Lett. **94**, 057003 (2005)
50. C.C. de Souza Silva, J. Van de Vondel, B.Y. Zhu, M. Morelle V.V. Moshchalkov, Phys. Rev. B **73**, 014507 (2006)
51. C.C. de Souza Silva, J. Van de Vondel, M. Morelle V.V. Moshchalkov, Nature **440**, 651 (2006)
52. P. Selders, R. Wördenweber, Appl. Phys. Lett. **76**, 3277 (2000)

53. R. Wördenweber, P. Selders, Physica C **366**, 135 (2002)
54. G.R. Berdiyorov, M.V. Milošević, F.M. Peeters, Qualitative modification of the pinning force due to vortex-cavity adherence in perforated superconducting films (unpublished)
55. G.S. Mkrtchyan, V.V. Shmidt, Sov. Phys. JETP **34**, 195 (1972)
56. A.I. Buzdin, D. Feinberg, Physica C **256**, 303 (1996)
57. P. Lahl, R. Wördenweber, Appl. Phys. Lett. **81**, 505 (2002)
58. A.N. Lykov, Solid State Commun. **86**, 531 (1993)
59. K. Harada, O. Kamimura, H. Kasai, T. Matsuda, A. Tonomura, V.V. Moshchalkov, Science **274**, 1167 (1996)
60. A. Bezryadin, Y.N. Ovchinikov, B. Pannetier, Phys. Rev. B **53**, 8553 (1996)
61. A. Bezryadin, B. Pannetier, J. Low Temp. Phys. **102**, 73 (1996)
62. V.V. Metlushko, U. Welp, G.W. Crabtree, Zhao Zhang, S.R.J. Brueck, B. Watkins, L.E. DeLong, B. Ilic, K. Chung, P.J. Hesketh, Phys. Rev. B **59**, 603 (1999)
63. V.V. Metlushko, U. Welp, G.W. Crabtree, R. Osgood, S.D. Bader, L.E. DeLong, Zhao Zhang, S.R.J. Brueck, B. Ilic, K. Chung, P.J. Hesketh, Phys. Rev. B **60**, R12585 (1999)
64. R. Wördenweber, E. Hollmann, J. Schubert, R. Kutzner, A.K. Ghosh, Appl. Phys. Lett. **94**, 202501 (2009)
65. B.Y. Zhu, L. Van Look, V.V. Moshchalkov, B.R. Zhao, Z.X. Zhao, Phys. Rev. B **64**, 012504 (2001)
66. F. Nori, Science **271**, 1373 (1996)
67. C. Reichhardt, C.J. Olson, F. Nori, Phys. Rev. B **57**, 7937 (1998)
68. C. Reichhardt, F. Nori, Phys. Rev. Lett. **82**, 414 (1999)
69. H. Nordborg, V.M. Vinokur, Phys. Rev. B **62**, 12408 (2000)
70. C.P. Bean, J.D. Livingston, Phys. Rev. Lett. **12**, 14 (1964)
71. K.K. Likharev, L.A. Yakobson, Sov. Phys. Tech. Phys. **20**, 950 (1976)
72. J. Schneider, H. Kohlstedt, R. Wördenweber, Appl. Phys. Lett. **63**, 2426 (1993)
73. J. Schneider, M. Mück, R. Wördenweber, Appl. Phys. Lett. **65**, 2475 (1994)
74. A. Andronov, I. Gordion, V. Kurin, I. Nefedov I. Shereshevsky, Physica C **213**, 193 (1993)
75. V.L. Ginzburg, L.D. Landau, Zh. Eksp. Teor. Fiz. **20**, 1064 (1950)
76. M. Tinkham, *Introduction to Superconductivity*, 2nd edn (McGraw-Hill, New York, 1996)
77. A. Weber L. Kramer, J. Low Temp. Phys. **84**, 289 (1991)
78. A. Andronov, I. Gordion, V. Kurin, I. Nefedov I. Shereshevsky, Physica C **213**, 193 (1993)
79. L.I. Glazman, Fiz. Nizk. Temp. **12**, 688 (1986); Sov. J. Low Temp. Phys. **12**, 389 (1986)
80. V.M. Fomin, R. Wördenweber, Proc. SPIE **7364**, 73640P (2009)
81. G.R. Berdiyorov, A.K. Elmurodov, F.M. Peeters D.Y. Vodolazov, Phys. Rev. B **79**, 174506 (2009)
82. A.I. Larkin, Y.N. Ovchinnikov, Zh. Eksp. Teor. Fiz. **68**, 1915 (1975); Sov. Phys. JETP **41**, 960 (1976)
83. S.G. Doettinger, R.P. Huebener, R. Gerdemann, A. Kühle, S. Anders, T.G. Träuble, J.C. Villégier, Phys. Rev. Lett. **73**, 1691 (1994); Physica C **235–240**, 3179 (1994)
84. P. Lahl, R. Wördenweber, Inst. Phys. Conf. Ser. **158**, 77 (1997)
85. L.E. Musienko, I.M. Dmitrenko, V.G. Volotskaya, Pis'ma Zh. Eksp. Teor. Fiz. **31**, 603 (1980); JETP Lett. **31**, 567 (1980)
86. W. Klein, R.P. Huebener, S. Gauss und J. Parisi, J. Low. Temp. Phys. **61**, 413 (1985)
87. S.G. Doettinger, R.P. Huebener, A. Kühle, Physica C **251**, 285 (1995)
88. R. Wördenweber, U. Krüger, J. Schneider, R. Kutzner, G. Ockenfuß, Inst. Phys. Conf. Ser. **148**, 619 (1995)
89. P. Selders, A.M. Castellanos, M. Vaupel, R. Wördenweber, Appl. Supercond. **5**, 269 (1998)
90. R. Surdeanu, R.J. Wijngaarden, R. Griessen, J. Einfeld, R. Wördenweber, Europhys. Lett. **54**, 682 (2001)
91. M. Pannetier, R.J. Wijngaarden, I. Fløan, J. Rector, R. Griessen, P. Lahl, R. Wördenweber, Phys. Rev. B **67**, 212501 (2003)
92. E.H. Brandt, Phys. Stat. Sol. B **77**, 551 (1976); J. Low Temp. Phys. **26**, 709, 735 (1977); J. Low Temp. Phys. **28**, 263, 291 (1977)

93. A. Lukashenko, A.V. Ustinov, A.P. Zhuravel, E. Hollmann, R. Wördenweber, J. Appl. Phys. **100**, 023913 (2006)
94. S.J. Hagen, C.J. Lobb, R.L. Greene, M.G. Forrester, J.H. Kang, Phys. Rev. B **41**, 11630 (1990)
95. S.J. Hagen, A.W. Smith, M. Rajeswari, J.L. Peng, Z.Y. Li, R.L. Greene, S.N. Mao, X.X. Xi, S. Bhattacharya, Qi Li, C.J. Lobb, Phys. Rev. B **47**, 1064 (1993)
96. P. Ao, J. Phys. Condens. Matter **10**, L677 (1998)
97. H.J. Jensen, P. Minnhagen, E. Sonin, H. Weber, Europhys. Lett. **20**, 463 (1992)
98. R.A. Ferrell, Phys. Rev. Lett. **68**, 2524 (1992)
99. A. van Otterlo, M. Feigel'man, V. Geshkenbein, G. Blatter, Phys. Rev. Lett. **75**, 3736 (1995)
100. D.I. Khomskii, A. Freimuth, Phys. Rev. Lett. **75**, 1384 (1995)
101. N.B. Kopnin, Phys. Rev. B **54**, 9475 (1996)
102. J. Kolacek, P. Vasek, Physica C **336**, 199 (2000)
103. R. Wördenweber, J.S.K. Sankarraj, P. Dymashevski, E. Hollmann, Physica C **434**, 101 (2006)
104. D. Koelle, R. Kleiner, F. Ludwig, E. Dantsker, J. Clarke, Rev. Mod. Phys. **71**, 631 (1999)
105. A.I. Braginski, H.J. Krause, J. Vrba, *Handbook of thin film devices, Superconducting Film Devices*, vol. 3, Academic, San Diego, pp. 149–225 (2000), ISBN: 0-12-408952-6
106. B.D. Josephson, Phys. Lett. **1**, 251 (1962)
107. M.B. Ketchen, W.J. Gallagher, A.W. Kleinsasser, S. Murphy, J.R. Clem, in *SQUID'85 – Superconducting Quantum Interference Devices and Their Applications*, ed. by H.D. Hahlbohm, H Lübbig (deGruyter, Berlin, 1985), p. 865ff
108. R. Gross, B. Mayer, Physica C **180**, 235 (1991)
109. M. Kawasaki, P. Chaudhari, A. Gupta, Phys. Rev. Lett. **68**, 1065 (1992)
110. A. Marx, R. Gross, Appl. Phys. Lett. **70**, 120 (1997)
111. A.H. Miklich, J. Clarke, M.S. Colclough, K. Char, Appl. Phys. Lett. **60**, 1899 (1992)
112. R.L. Forgacs, A.F. Warwick, Rev. Sci. Instrum. **38**, 214 (1967)
113. V. Foglietti, W.J. Gallagher, M.B. Ketchen, A.W. Kleinsasser, R.H. Koch, S.I. Raider, R.L. Sandstrom, Appl. Phys. Lett. **49**, 1393 (1986)
114. R.H. Koch, J. Clarke, W. M. Goubau, J. M. Martinis, C. M. Pegrum, D. J. van Harlingen, J. Low Temp. Phys. **51**, 207 (1983)
115. R.H. Koch, W. Eidelloth, B. Oh, R.P. Robertazzi, S.A. Andrek, W.J. Gallagher, Appl. Phys. Lett. **60**, 507 (1992)
116. A.H. Miklich, D. Koelle, E. Dantsker, D.T. Nemeth, J.J. Kingston, R.F. Kromann, J. Clarke, IEEE Trans. Appl. Supercond. **3**, 2434 (1993)
117. M. Mück, C. Heiden, J. Clarke, J. Appl. Phys. **75**, 4588 (1994)
118. P. Dutta, P. Dimon, P.M. Horn, Phys. Rev. Lett. **60,** 646 (1979)
119. P. Dutta, P.M. Horn, Rev. Mod. Phys. **53**, 497 (1981)
120. M.J. Ferrari, M. Johnson, F.C. Wellstood, J.J. Kingston, T.J. Shaw, J. Clarke, J. Low Temp. Phys. **94**, 15 (1994)
121. E. Dantsker, S. Tanaka, J. Clarke, Appl. Phys. Lett. **70**, 2037 (1997)
122. R.H. Koch, J.Z. Sun, V. Foglietta, W.J. Gallagher, Appl. Phys. Lett. **67**, 709 (1995)
123. T.J. Shaw, J. Clarke, R.B. van Dover, L.F. Schneemeyer, A.E. White, Phys. Rev. **B54**, 15411 (1996)
124. J.R. Clem, Vortex exclusion from superconducting strips and SQUIDs in weak perpendicular ambient magnetic fields (unpublished) (1998)
125. H.J. Chaloupka, in *Microwave Application of High Temperature Superconductors, NATO ASI Series*, ed. by H. Weinstock (Kluwer, Dordrecht) (1999)
126. H.J. Chaloupka, M. Jeck, B. Gurzinski, S. Kolesov, Electron. Lett. **32**, 1735 (1996)
127. I.B. Vendik, O.G. Vendik, D.I. Kaparkov, Superconductor Microwave Technology, Part II: Superconducting Microwave Circuits, Chalmers University of Technology, Report No. 24, ed. by E. Kollberg, ISSN: 1103-4599, ISRN CTH-MVT-R-24–SE (1996)
128. M. Baziljevich, T.H. Johansen, H. Bratsberg, Y. Shen P. Vase, Appl. Phys. Lett. **69** 3590 (1996)
129. V.V. Yurchenko, R. Wördenweber, Yu. M. Galperin, D.V. Shantsev, J.I. Vestgården, T.H. Johansen, Physica C **437–438**, 357 (2006)

130. R.P. Feynman, R.B. Leighton M. Sands, *The Feynman Lectures on Physics*, vol. I (Addison-Wesley, Reading, 1963)
131. M. Smoluchowski, Phys. Z. **13**, 1069 (1912)
132. E. Kay, D. Leigh F. Zerbetto, Angew. Chem. Int. **46**, 72 (2007)
133. T. Omabegho, R. Sha N.C. Seeman, Science **324**, 67 (2009)
134. Y. Hiratsuka, T. Tada, K. Oiwa, T. Kanayama T. Uyeda, Biophys. J. **81**, 1555 (2001)
135. H. Linke, T.E. Humphrey, A. Löfgren, A.O. Sushkov, R. Newbury, R.P. Taylor P. Omling, Science **286**, 2314 (1999)
136. D.E. Shalóm H. Pastoriza, Phys. Rev. Lett. **94**, 177001 (2005)

http://www.springer.com/978-3-642-15136-1

Nanoscience and Engineering in Superconductivity
Moshchalkov, V.; Woerdenweber, R.; Lang, W. (Eds.)
2010, XVIII, 395 p., Hardcover
ISBN: 978-3-642-15136-1